Comparative analysis of spread-F signature and GPS scintillation occurrences at Tucumán, Argentina

L. Alfonsi,[1] L. Spogli,[1] M. Pezzopane,[1] V. Romano,[1] E. Zuccheretti,[1] G. De Franceschi,[1] M. A. Cabrera,[2,3,4] and R. G. Ezquer[3,4,5]

Received 19 December 2012; revised 15 May 2013; accepted 3 June 2013; published 1 July 2013.

[1] We analyze data recorded from October 2010 to September 2011, during the ascending phase of the 24th solar cycle, from an Advanced Ionospheric Sounder-Istituto Nazionale di Geofisica e Vulcanologia ionosonde and a GPS Ionospheric Scintillation and total electron content (TEC) monitor scintillation receiver, colocated at low latitude in the Southern American longitudinal sector (Tucumán, 26.9°S, 294.6°E, magnetic latitude 15.5°S, Argentina). The site offers the opportunity to perform spread-F and GPS scintillation statistics of occurrence under the southern crest of the equatorial ionospheric anomaly. Spread-F signatures, classified into four types (strong range spread-F (SSF), range spread-F, frequency spread-F (FSF), and mixed spread-F), the phase and amplitude scintillation index (σ_Φ and S_4, respectively), the TEC, and the rate of TEC parameter, marker of the TEC gradients, that can cause scintillations, are considered. The seasonal behavior results as follows: the occurrence of all four types of spread-F is higher in summer and lower in winter, while the occurrence of scintillations peaks at equinoxes in the postsunset sector and shows a minimum in winter. The correspondence between SSF and scintillations seems to be systematic, and a possible correlation between S_4 and FSF peaks is envisaged at the terminator. The investigation focused also on two particular periods, from 12 to 16 March 2011 and from 23 to 29 September 2011, both characterized by the simultaneous presence of SSF signatures and scintillation phenomena, allowing to discuss the role of traveling ionospheric disturbances as a strong candidate causing ionospheric irregularities.

Citation: Alfonsi, L., L. Spogli, M. Pezzopane, V. Romano, E. Zuccheretti, G. De Franceschi, M. A. Cabrera, and R. G. Ezquer (2013), Comparative analysis of spread-F signature and GPS scintillation occurrences at Tucumán, Argentina, *J. Geophys. Res. Space Physics*, *118*, 4483–4502, doi:10.1002/jgra.50378.

1. Introduction

[2] A deep understanding of the temporal and spatial evolution of the ionosphere can be achieved only by using a multi-instrument approach which provides complementary information. Bearing this in mind, we considered data from ionosonde soundings and GPS high rate samplings recorded in Tucumán (26.9°S, 294.6°E, magnetic latitude 15.5°S), Argentina. The site is particularly interesting for its location, near the southern crest of equatorial ionospheric anomaly [e.g., *Kelley*, 1989]. At equatorial latitudes, the magnetic field **B** is nearly parallel to the Earth's surface, and, during daytime, the *E* region dynamo electric field **E** is eastward. The resulting **E** × **B** drift transports *F* region plasma upward at the magnetic equator. The uplifted plasma then moves along **B** lines in response to gravity and pressure-gradient forces. As a result, the equatorial anomaly is formed with minimum *F* region ionization density at the magnetic equator and maxima at the two crests, approximately 15°–20° in magnetic latitude to the north and south. This electrodynamic mechanism is known as the equatorial "fountain effect." Near sunset, plasma densities and dynamo electric fields in the *E* region decrease and the equatorial anomaly begins to weaken. However, at this local time, a dynamo develops in the *F* region. Polarization charges within conductivity gradients at the terminator enhance the eastward electric field after sunset. The postsunset electric field moves the ionospheric plasma upward, allowing the equatorial anomaly crests to intensify. In these hours, a rapid uplifting of the *F* region and the steepening of the bottom side gradient lead to the Rayleigh-Taylor (R-T) instability [e.g., *Jin et al.*, 2008]. The instability allows plasma density

[1]Istituto Nazionale di Geofisica e Vulcanologia, Rome, Italy.
[2]Laboratorio de Telecomunicaciones, DEEC, FACET, Universidad Nacional de Tucumán, Tucumán, Argentina.
[3]Laboratorio de Ionósfera, Departamento de Física, FACET, Universidad Nacional de Tucumán, Tucumán, Argentina.
[4]CIASUR, Facultad Regional Tucumán, Universidad Tecnológica Nacional, Tucumán, Argentina.
[5]Consejo Nacional de Investigaciones Científicas y Técnicas, Buenos Aires, Argentina.

Corresponding author: L. Alfonsi, Istituto Nazionale di Geofisica e Vulcanologia, Via di Vigna Murata 605, Rome IT-00143, Italy. (lucilla.alfonsi@ingv.it)

2169-9380/13/10.1002/jgra.50378

irregularities to form. These irregularities can grow to become large ionospheric depletions often called "equatorial plasma bubbles." During a storm/substorm development phase, electric fields promptly penetrate from auroral to equatorial latitudes with eastward polarity in the sunset sector, causing enhanced instability growth and equatorial spread-F (ESF) development. The auroral electrojet (*AE*) recovery associated with the interplanetary magnetic field component B_z turning north, which accompanies large westward electric field, guarantees stability of the *F* region that otherwise would be unstable. Late night ESF activity can be disrupted by penetrating electric field of westward polarity arising from *AE* activity [*Abdu et al*., 2009; *Muella et al*., 2010].

[3] Signatures of the irregularities growth are clearly visible in the high-frequency (HF) vertical soundings and in the GPS signal samplings. In fact, the HF echoes received at ground are in these cases characterized by a pronounced spread of the *F* region echo (spread-F). Hence, although spread-F conditions represent an impediment to perform an accurate scaling of an ionogram, it gives valuable information on the occurrence, both geographical and temporal, of *F* region irregularities [e.g., *Abdu et al*., 2012]. From a GPS point of view, as radio waves propagate through irregularities in the ionosphere, they experience different values of TEC (total electron content), resulting in group delay and phase advance, which are referred to as refraction [e.g., *Yeh and Liu*, 1982; *Cerruti et al*., 2008]. Diffraction arises when ionospheric irregularities form at scale lengths of about 400 m and begin to scatter GPS signals. Refraction and diffraction effects result into fluctuations of the phase and amplitude of the signal received at ground called scintillations. At low latitude, scintillations are regularly recorded in the postsunset hours and enhanced or suppressed under geomagnetic disturbed conditions. In a recent paper, *Alfonsi et al*. [2011a] have shown how TEC looks like when scintillations increase or inhibit. In the former case, large electron density depletions (i.e., bubbles) appear, and in the latter case, TEC varies smoothly in time and space. Geomagnetic storms can also affect the motion of the neutral atmosphere traced by the modulation of the background ionization through the traveling ionospheric disturbances (TIDs). Traveling ionospheric disturbances are essentially the manifestation of atmospheric gravity waves (GWs) in the ionosphere [*Hines*, 1959]. According to their different wavelengths (scales), there is a classification of three different types of TIDs [e.g., *Leitinger and Rieger*, 2005]:

[4] 1. Large-scale TIDs (LSTIDs) with their origin in the auroral zone, with horizontal wavelengths greater than 1000 km, periods ranging from 30 min to 3 h and horizontal phase velocities of 300–1000 m/s.

[5] 2. Medium-scale TIDs (MSTIDs) with origins mostly in the lower atmosphere and also in the auroral zone. Horizontal wavelengths from 100 to 300 km, periods from about 12 min to 1 h and horizontal phase velocities from 100 to 300 m/s.

[6] 3. Small-scale TIDs (SSTIDs) with origins only in the lower atmosphere. The corresponding wavelengths, velocities, and periods are smaller than those of MSTIDs, because they belong to the acoustic branch.

[7] We will see in section 3 that under geomagnetically unstable conditions, MSTIDs seem to play an important role in causing irregularities responsible for both spread-F and scintillation records.

[8] Besides analyzing two specific periods of March and September 2011, in this paper, we describe the statistical study derived by the analysis of the observations, acquired between October 2010 and September 2011, of ESF, TEC, and scintillations variability. Solicited by the work of *Shi et al*. [2011], which identifies the correspondence between strong range spread-F (SSF) and scintillations occurrence, we introduce, for the first time, close to the southern crest of the equatorial ionospheric anomaly, a detailed comparison between the occurrence of different types of ESF and the occurrence of the amplitude/phase scintillations, considering also TEC and relative TEC conditions. In the South American sector, previous similar analyses were done only at the magnetic equator [*Iyer et al*., 2003; *Rodrigues et al*., 2004; *Chen et al*., 2006; *Li et al*., 2011], and in other longitudinal sectors, they were done either at the magnetic equator or at the northern crest of the equatorial ionospheric anomaly [*Huang*, 1970; *Lee et al*., 2009; *Bagiya and Sridharan*, 2011; *Chen et al*., 2011; *Shi et al*., 2011; *Tsunoda et al*., 2011]. Additionally, the two case studies, besides giving new insights on the role of TIDs, highlight at the same time the close relation between ESF and scintillations occurrence.

2. Data and Method

[9] The data considered for the present study are those recorded by an ionosonde and a GPS receiver, owned by INGV (Istituto Nazionale di Geofisica e Vulcanologia) and hosted by the Facultad Regional de Tucumán of the Universidad Tecnologica Nacional at San Miguel de Tucumán, approximately 1000 km northwest from Buenos Aires, Argentina. The period under investigation goes from October 2010 to September 2011, characterized by an increasing low-medium solar activity, with the R_{12} index ranging from 23 to 60 (http://www.ngdc.noaa.gov/stp/iono/sunspot.html). The ionosonde is an AIS-INGV (Advanced Ionospheric Sounder-Istituto Nazionale di Geofisica e Vulcanologia), developed and built at INGV in Rome [*Zuccheretti et al*., 2003], while the GPS receiver is a GSV4004 GPS Ionospheric Scintillation TEC monitor (GISTM) that consists of a NovAtel OEM4 dual-frequency receiver.

[10] The sounding repetition rate and sweeping frequency range of the AIS-INGV ionosonde were set to 5 min and from 1.5 to 19.0 MHz, respectively. Spread-F signatures recorded by the ionosonde were classified into four types: frequency spread-F (FSF), mixed spread-F (MSF), and range spread-F (RSF) according to the description given by *Piggott and Rawer* [1972] in their *URSI Handbook of Ionogram Interpretation and Reduction*, and strong range spread-F (SSF) defined according to *Shi et al*. [2011]. Figures 1a–1d show an example for each of the different types of spread-F just mentioned. Spread-F echoes provide information on the distribution of irregularities: FSF ionogram traces represent irregularities located near the *F* region peak; RSF ionogram traces represent irregularities located mainly at the bottomside of the *F* region; MSF ionogram traces represent irregularities located throughout the *F* region. SSF ionogram traces are instead characterized by an extended range spread-F echo that significantly extends well past the critical frequency of the

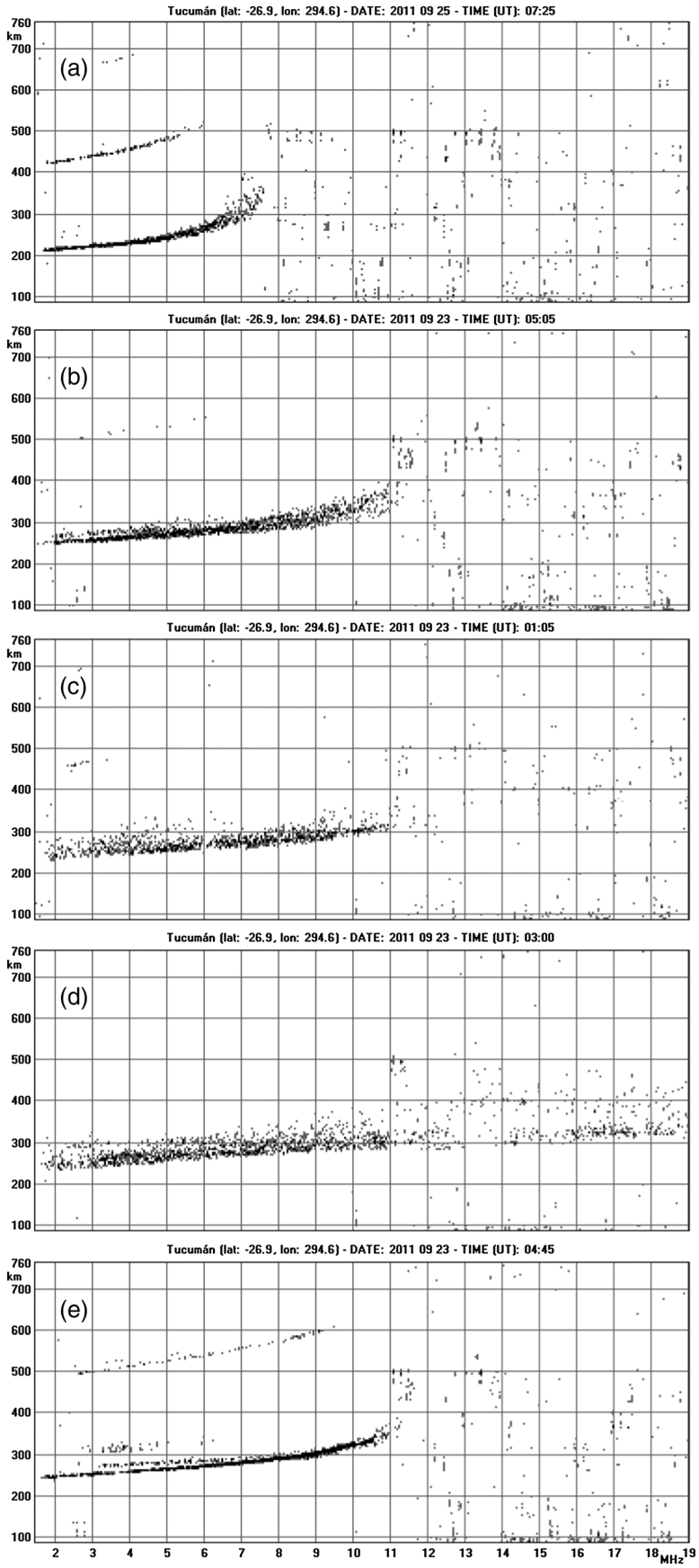

Figure 1. Examples of ionograms showing (a) frequency spread-F, (b) mixed spread-F, (c) range spread-F, (d) strong range spread-F, and (e) satellite trace.

F region (f_oF_2), covering the whole ionosonde frequency range. As described by *Shi et al*. [2011], for SSF conditions, the bottomside depletions reach the topside ionosphere where they are generally classified as plumes [e.g., *Kelley*, 1989]. In this situation, field-aligned F region irregularities at the walls of the depletions produce strong coherent backscatter that appears as SSF on the ionograms [*Sales et al*., 1996]. Figure 1e is an example of ionogram showing the presence of satellite traces (STs) that is one or more quasi-replicas of the main ionogram trace at displaced virtual heights. Satellite traces are probably produced by oblique reflections from corrugations in the isodensity surfaces caused by GW propagation [*Tsunoda*, 2008]. We take care of recording also such ionogram feature in order to confirm what it was already found by *Cabrera et al*. [2010], who showed that RSF occurrence at Tucumán, heralded tens of minutes in advance by ST appearance, seems to be related to GW propagation through the F region. In order to detect the different types of spread-F and ST signatures on the ionogram, reference was made to the visualization feature of the electronic Space Weather upper atmosphere database (http://www. eswua.ingv.it/) [*Romano et al*., 2008].

[11] The ionospheric scintillations are observed by a GISTM, a special GPS receiver which includes a dedicated firmware able to compute in near real time, from 50 Hz samplings, the amplitude and the phase scintillation from the GPS L1 (1575.42 MHz) frequency signal and TEC from the GPS L1 and L2 (1227.60 MHz) carrier phase signals.

[12] The receiver provides the amplitude scintillation by computing the S_4 index, which is the standard deviation of the received power normalized by its mean value. In this case, it is derived from the detrended received signal intensity. A high-pass filter is used for detrending the raw amplitude measurements [*Van Dierendonck et al*., 1993]. A fixed choice of a 0.1 Hz 3 dB cutoff frequency for both phase and amplitude filterings is used. Phase scintillation computation is accomplished by monitoring the standard deviation of the detrended carrier phase, i.e. the σ_Φ index. A high-pass sixth-order Butterworth filter is used for detrending raw phase measurements. Both S_4 and σ_Φ are computed over 1, 3, 10, 30, and 60 s intervals. The receiver provides also TEC and rate of TEC (ROT) values computed over 15, 30, 45, and 60 s. In this analysis, we consider TEC and scintillation indices calculated over 60 s. In order to account for varying geometrical effects on the measurements made at different elevation angles, the scintillation indices and the TEC are projected to the vertical according to the following formulae:

$$S_4^{\text{vert}} = \frac{S_4^{\text{slant}}}{(F(\alpha_{\text{elev}}))^b}, \tag{1}$$

$$\sigma_\Phi^{\text{vert}} = \frac{\sigma_\Phi^{\text{slant}}}{(F(\alpha_{\text{elev}}))^a}, \tag{2}$$

$$v\text{TEC} = \frac{s\text{TEC}}{F(\alpha_{\text{elev}})}, \tag{3}$$

where $\sigma_\Phi^{\text{slant}}$, S_4^{slant}, and sTEC are the scintillation indices and TEC directly provided by the receiver at a given elevation angle (α_{elev}) along the slant path. $\sigma_\Phi^{\text{vert}}$, S_4^{vert}, and vTEC are the corresponding values projected to the vertical. $F(\alpha_{\text{elev}})$ is the obliquity factor that is defined as [*Mannucci et al*., 1993]

$$F(\alpha_{\text{elev}}) = \frac{1}{\sqrt{1 - \left(\frac{R_E \cos \alpha_{elev}}{R_E + H_{IPP}}\right)^2}} \tag{4}$$

where R_E is the Earth radius and H_{IPP} is the height of the ionospheric piercing point (IPP). According to the formula (19) of *Rino* [1979], which describes the signal phase variance as a function of the zenith angle, and as described by *Spogli et al*. [2009], the exponent a of equation (2) is assumed to be 0.5. The exponent b of equation (1) depends on the spectral index p of the phase scintillation spectrum and on the anisotropy of the irregularity. In agreement with *Spogli et al*. [2009], the value is reasonably chosen to be $p = 2.6$, corresponding to $b = 0.9$. For further details on the dependence of scintillation indices on the elevation angle, the reader is referred also to page 113 of *Wheelon* [2003]. Hereafter, we refer to $\sigma_\Phi{}^{\text{vert}}$ and $S_4{}^{\text{vert}}$ as σ_Φ and S_4, respectively.

[13] In order to complete the statistics on the ionospheric environment observed from Tucumán with the information related to the electron density gradients, we analyzed also the ROT changes, computed over 1 min intervals, calculating the difference between the relative (slant) TEC values provided by the GISTM receiver.

[14] Generally, in order to reduce the impact of nonscintillation-related tracking errors (such as multipath), only observations acquired at elevation angles greater than 20° are considered. In this work, a more severe filter is applied to match the field of view of the receiver with the coverage of the vertical sounding carried out by the ionosonde, thus we consider GPS satellites in view from 60° over the horizon, as sketched in Figure 2. White circle in Figure 2b shows such field of view simultaneously spanned by the GPS receiver and by the ionosonde located at San Miguel de Tucumán, while the yellow curve indicates the averaged position of the magnetic equator.

[15] The statistics of the GPS data is obtained by means of the Ground Based Scintillation Climatology (GBSC) technique, an original tool developed by INGV, which enables the identification of the main areas of the ionosphere in which scintillation is more likely to occur. The GBSC builds maps of the percentage of occurrence and/or of mean and standard deviation of scintillation indices, TEC, signal-to-noise ratio, and other parameters defined in a bidimensional coordinates system (geographic coordinates, geomagnetic coordinates, horizontal coordinates, time) selected on demand. Details on the method can be found in *Spogli et al*. [2009]. As the encouraging results recently achieved in drawing the scintillation climatology over both the poles [*Alfonsi et al*., 2011b], the same method is here applied to assess the low-latitude scintillation recurrence.

[16] Only few gaps of GISTM date are present in the whole considered period (October 2010 to September 2011), in fact, data are available for 98.9% of the days. About 4.45 million of 1 min scintillation data are recorded, even if only 15% (~670·000 data) of them falls into the common field of view of GISTM and ionosonde (60° in elevation) considered in this study.

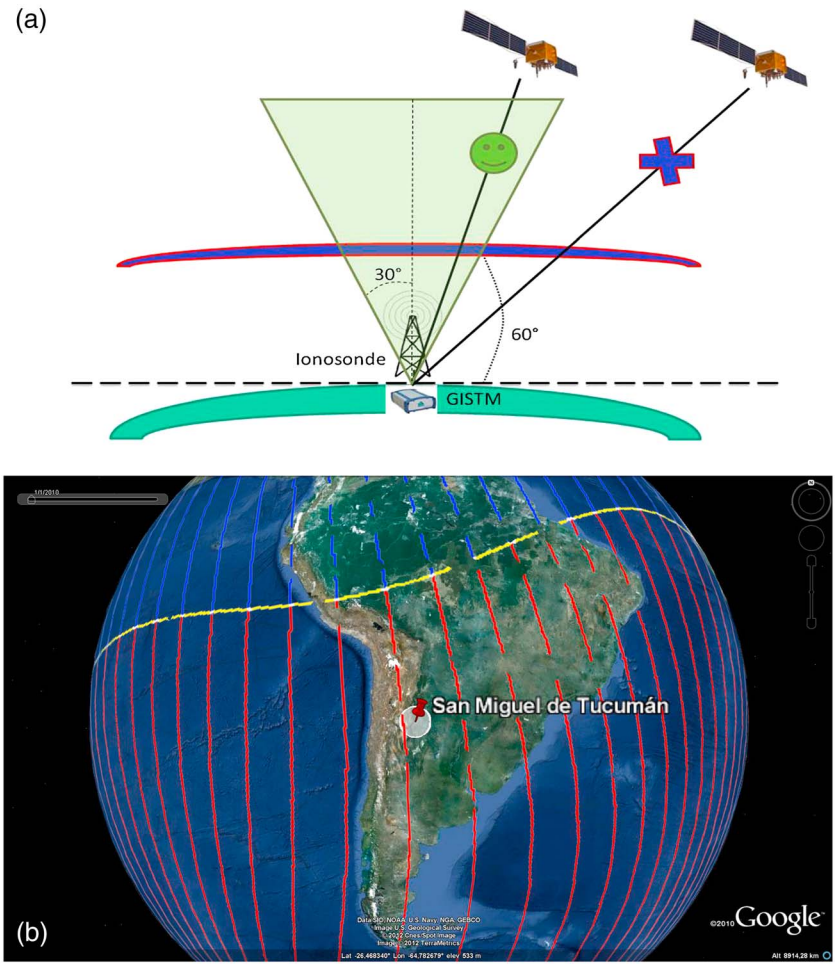

Figure 2. (a) The elevation angle considered in this study. (b) Field of view covered by the GPS receiver according to the 60° threshold chosen for the elevation angle and by the ionosonde located at Tucumán (white circle). The yellow curve indicates the averaged position of the magnetic equator.

3. Results

[17] Data acquired between October 2010 and September 2011 were analyzed to (1) compare the different types of ESF appearance with scintillation occurrence; (2) compare RSF, ST, and scintillation occurrences; and (3) investigate two specific case studies both characterized by SSF and scintillations.

3.1. Statistical Comparison Between ESF and Scintillation Occurrences

[18] Figures 3a–3c describe the ESF and scintillations monthly occurrence, also sorted by time to characterize the premidnight hours (between 18:00 LT and 00:00 LT) and the postmidnight hours (between 00:00 LT and 06:00 LT). Once a specific month is considered, the ESF percentage of occurrence is calculated as the number of days for which an ESF type was identified divided by the total number of days for which the data are available. When sorting by time, only the ionograms recorded, respectively, between 18:00 LT and 00:00 LT, and between 00:00 LT and 06:00 LT, are considered.

[19] The percentage occurrence of scintillation (O_{scint}) is here calculated according to the following formula:

$$O_{\text{scint}} = \frac{N_{\text{thr}}}{N_{\text{tot}}}. \tag{5}$$

[20] Once a specific month is considered, N_{thr} and N_{tot}, both of them evaluated for $\alpha_{\text{elev}} \geq 60°$, represent, respectively, the number of data points corresponding to the given scintillation index above threshold and the total number of data points. In our study, we consider as amplitude and phase scintillation events those for which S_4 and σ_Φ are above 0.25 and 0.25 rad, respectively. Similar to other authors [e.g., *Beniguel et al.*, 2009; *Li et al.*, 2010], such thresholds are considered as moderate/strong scintillation thresholds.

[21] Figures 3d–3f show the hourly daily variation of the occurrences sorted by seasons, which are defined as follows: equinoxes (March, April, September, and October), winter (May, June, July, and August), and summer (November, December, January, and February). Once a specific season is considered, the hourly ESF percentage of occurrence is calculated as the number of days for which the corresponding

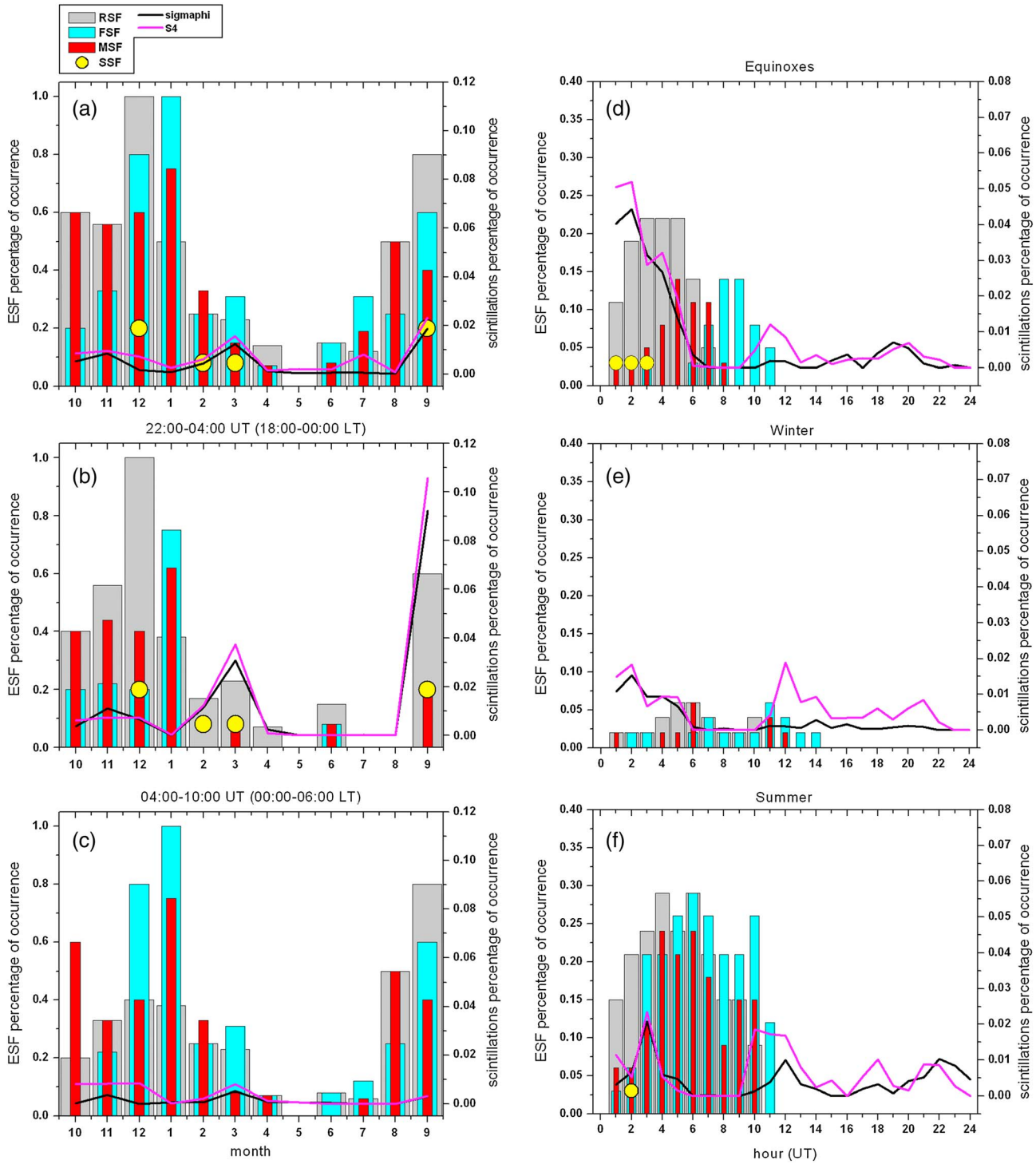

Figure 3. RSF (gray bar), FSF (cyan bar), MSF (red bar), SSF (yellow circles), amplitude (magenta curve) and phase (black curve) scintillation monthly occurrence (a) for 24 h of the day, (b) for premidnight hours, and (c) for postmidnight hours. RSF, FSF, MSF, SSF, and amplitude and phase scintillation hourly occurrence (d) at equinoxes, (e) in winter, and (f) in summer.

ESF type is detected between *h*:00 UT and *h*:55 UT (where *h* is the hour) divided by the total number of days for which the data are available, while the scintillation occurrence O_{scint} is calculated according to formula (5) by taking into account data points recorded between *h*:00 UT and *h*:55 UT.

[22] The occurrence of all four types of spread-F is higher in summer and lower in winter, while the occurrence of scintillations presents a peak at equinoxes in the postsunset sector and a minimum in winter. ESF signatures are a nocturnal phenomenon, while scintillations are present all day long;

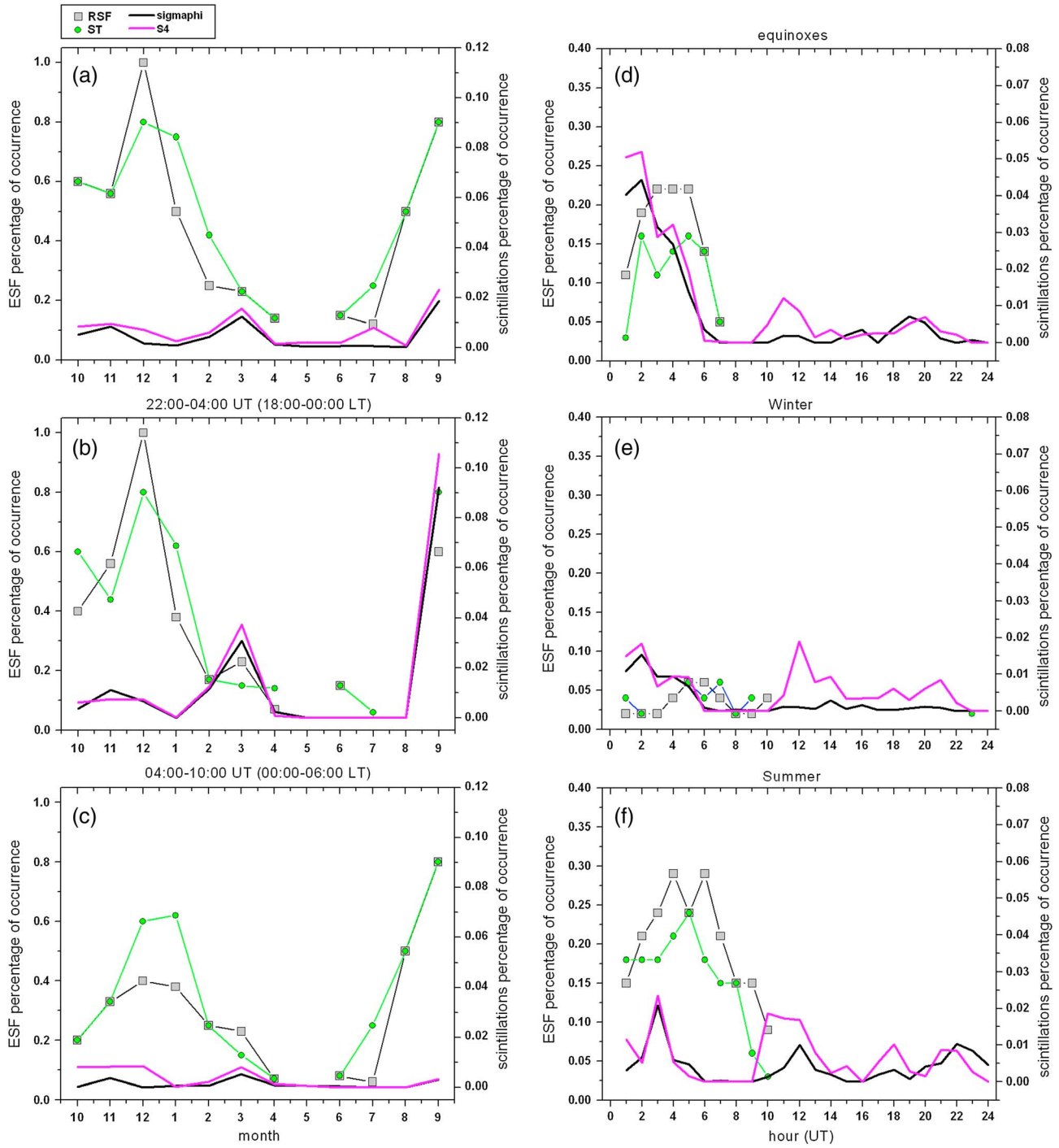

Figure 4. RSF (gray squares), ST (green circles), and amplitude (magenta curve) and phase (black curve) scintillation monthly occurrence (a) for 24 h of the day, (b) for premidnight hours, and (c) for postmidnight hours. RSF, ST, and amplitude and phase scintillation hourly occurrence (d) at equinoxes, (e) in winter, and (f) in summer.

all the seasons show a deviation of S_4 from σ_Φ between 10:00 UT and 13:00 UT (06:00–09:00 LT), in winter such deviation being slightly delayed. As observed in the order of magnitude (right-hand y axis) of the monthly percentage of occurrence, scintillations over Tucumán are recorded mainly in the premidnight hours.

[23] During the equinoxes and in summer, the SSF incidence is signed by a scintillations enhancement, both in phase and in amplitude. Moreover, SSF results to be a premidnight phenomenon. During winter, SSF phenomena are not recorded.

[24] It is interesting to note a possible correspondence between the FSF incidence and the deviation of scintillation indices occurrence, especially S_4, in the postmidnight hours and preferably during the equinoxes. This correspondence seems to be favored around 10:00–11:00 UT (06:00–07:00 LT) and

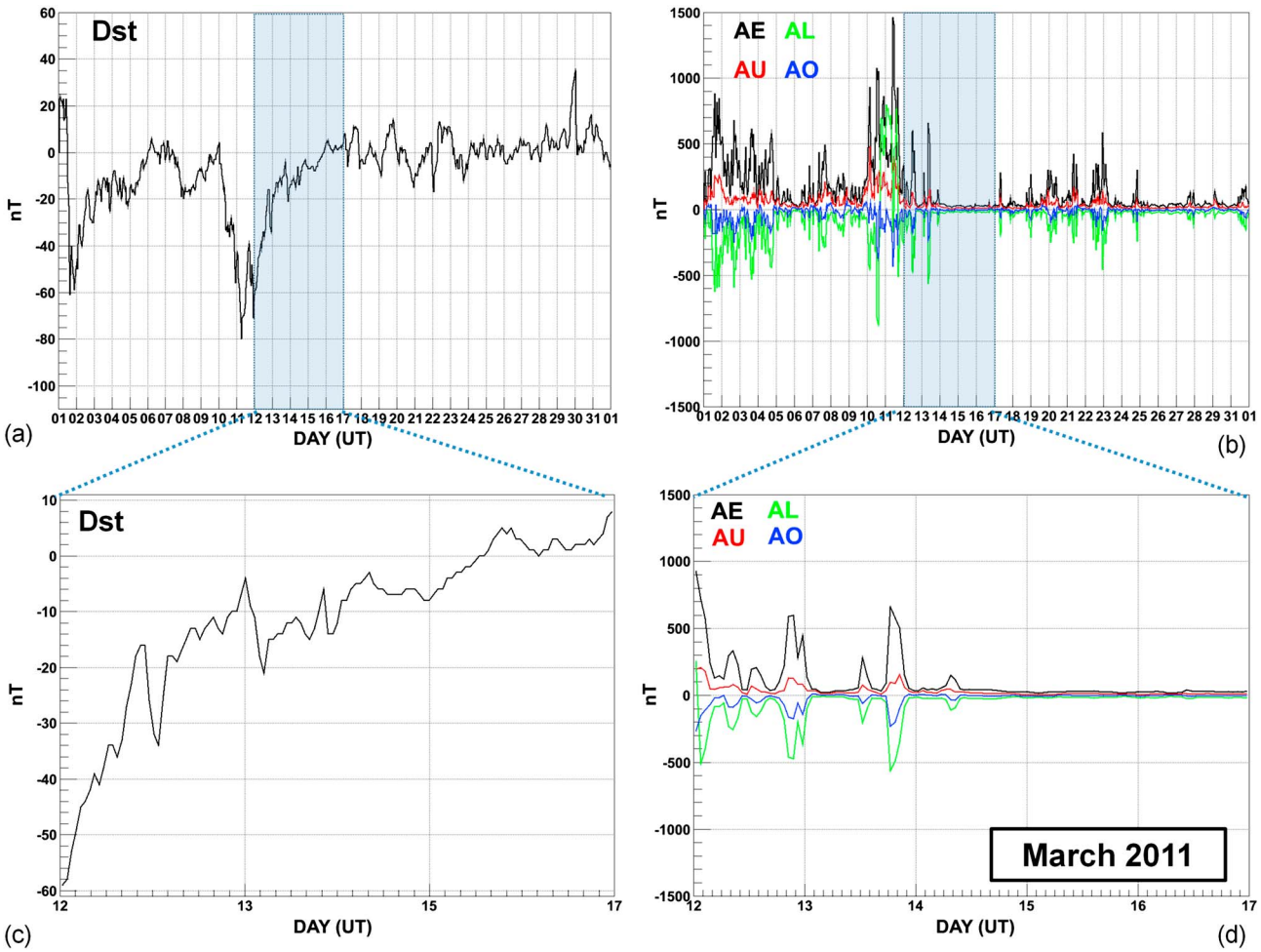

Figure 5. (a, c) *Dst* and (b, d) *AE*, *AL*, *AU*, and *AO* indices recorded in March 2011. The days from 12 to 16 March investigated in the work are shaded in Figures 5a and 5b and zoomed-in details in Figures 5c and 5d, respectively.

shifted to later time in winter (peak on 12:00 UT or 08:00 LT). An anticorrelation between the MSF type occurrence and scintillations appearance is also marked in all seasons, with clear evidence at equinoxes and in summer. The bulk of the scintillation occurrence during the equinoxes is concentrated in the postsunset/premidnight sector when SSF is often observed.

3.2. Statistical Comparison Between RSF, ST, and Scintillation Occurrences

[25] As STs can be considered as precursors to the appearance of an RSF trace on the ionograms, Figure 4 reports the ST and RSF variations, showing that they are practically in phase. Figure 4 shows that both for the monthly and for the seasonal variations, when ST and/or RSF are visible on the ionogram, an increase of the scintillations indices, mainly on the signal amplitude, often occurs. This is particularly evident in the equinoctial plot (Figure 4d) and in the monthly variation in the premidnight sector (Figure 4b). The increase of S_4 centered around 10:00–13:00 UT and present during all the seasons (Figures 4d–4f) does not correspond to any RSF/ST.

3.3. Case Studies: Two Geomagnetically Unstable Periods in March and September 2011 Both Characterized by SSF and Scintillations

[26] The storm occurred between 10 and 16 March 2011 is described by the geomagnetic conditions reported in Figure 5 in which the time evolution of *Dst* (Figure 5a), *AE*, *AL*, *AU*, and *AO* (Figure 5b) indices is plotted. The *Dst* index [e.g., *Mayaud*, 1980] shows a depression till about −80 nT on 11 March and several substorms occurring during the initial and recovery phases. Signatures of these substorms are clearly visible in the *AE* [*Davis and Sugiura*, 1966] variation, presenting significant perturbations, till deviations of 1000 nT (Figure 5b).

[27] Simultaneous ionosonde and GISTM data availability allowed a complementary investigation of the scintillations and ESF occurrence only during the recovery phase of the storm from 12 to 16 March. Figures 6a–6e report S_4, σ_Φ, *v*TEC, and ROT changes recorded during each day of this period; on the same plots, the ESF occurrence is highlighted with different colors. On 12 March, the level of postsunset scintillation increases significantly (Figure 6a) and lasts from 00:00 UT to about 03:00 UT (20:00–23:00 LT on 11 March),

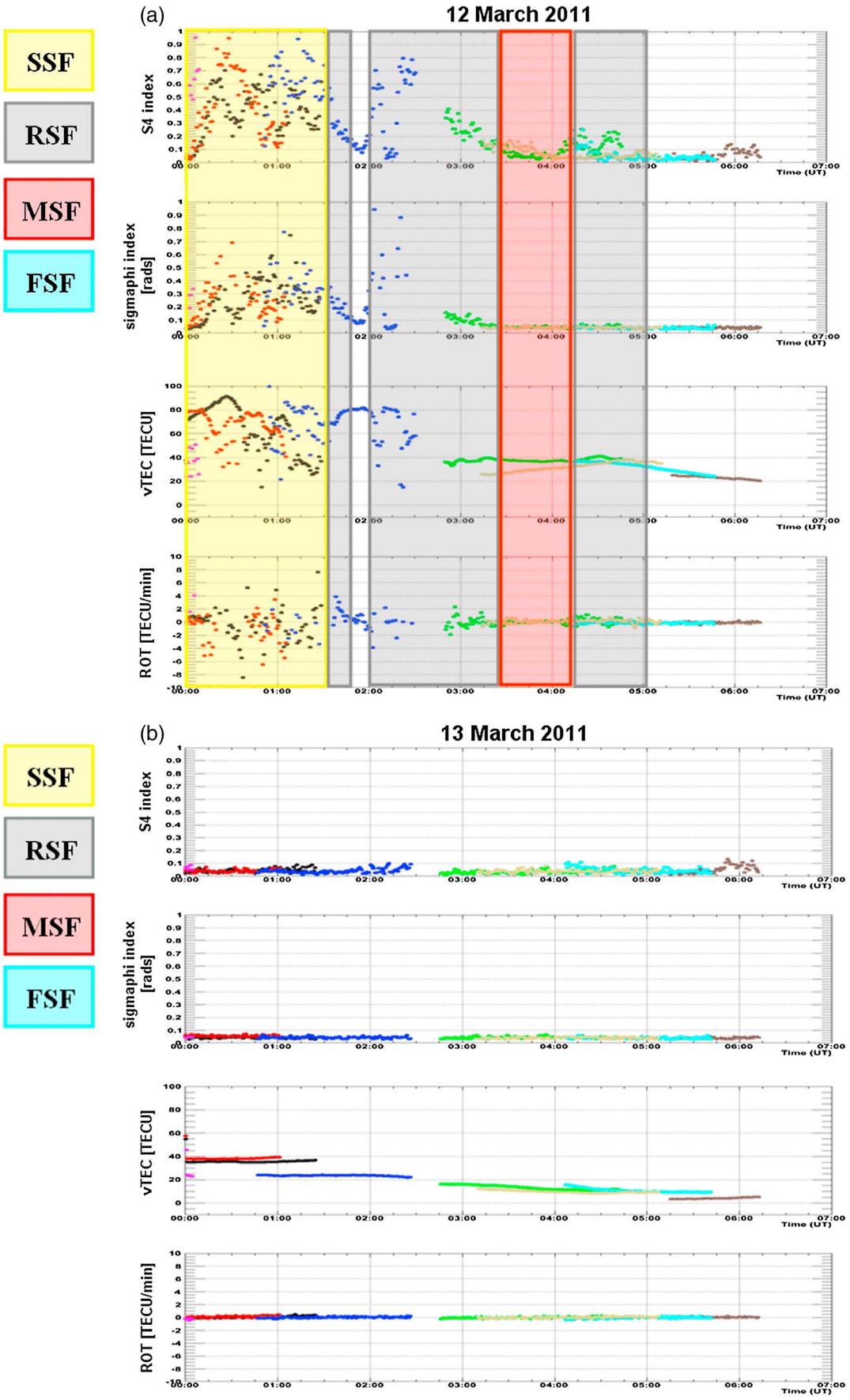
(a)
12 March 2011
SSF
RSF
MSF
FSF
S4 index
sigmaphi index [rads]
vTEC [TECU]
ROT [TECU/min]
Time (UT)
(b)
13 March 2011
SSF
RSF
MSF
FSF
S4 index
sigmaphi index [rads]
vTEC [TECU]
ROT [TECU/min]
Time (UT)

Figure 6

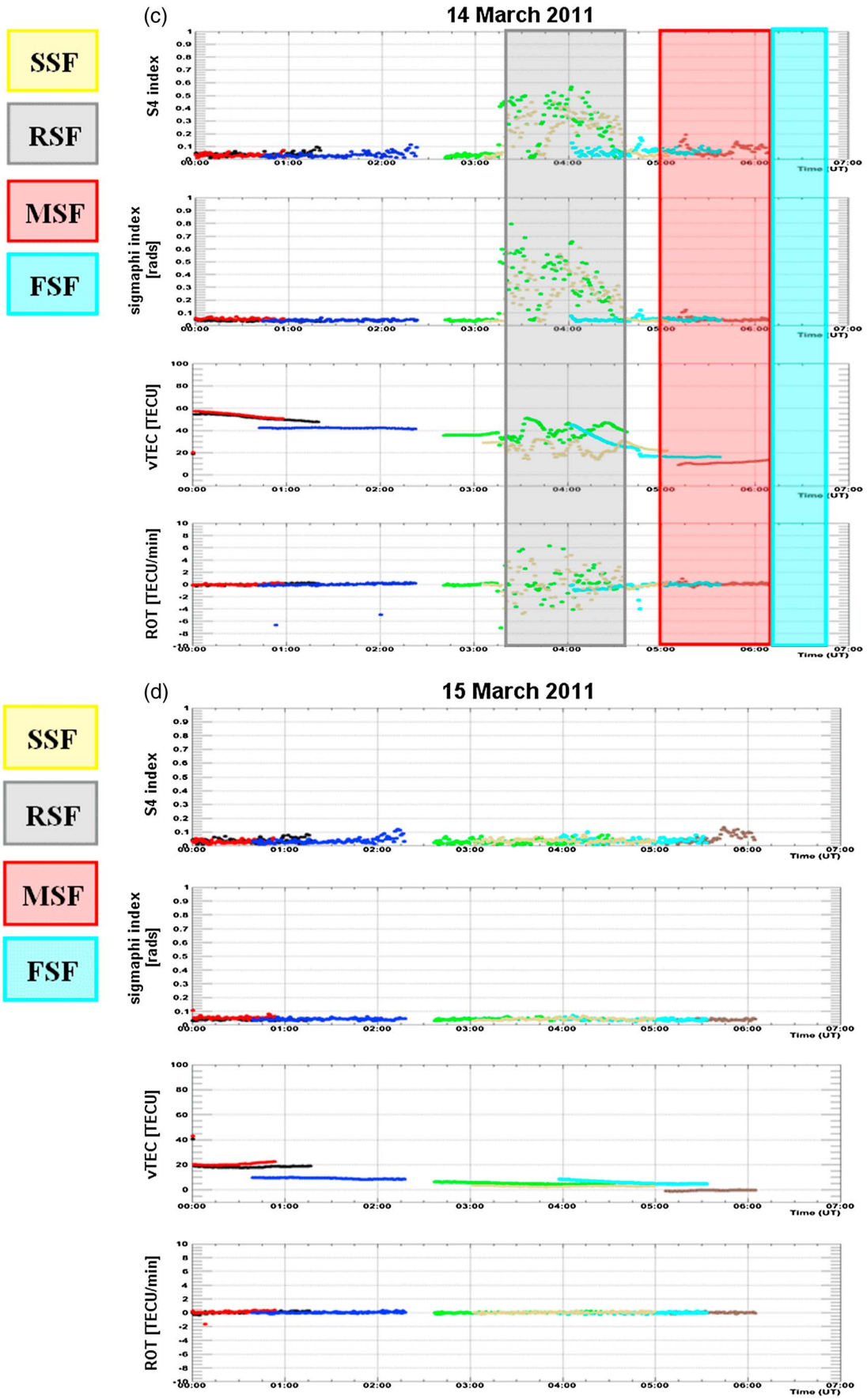

Figure 6. (continued)

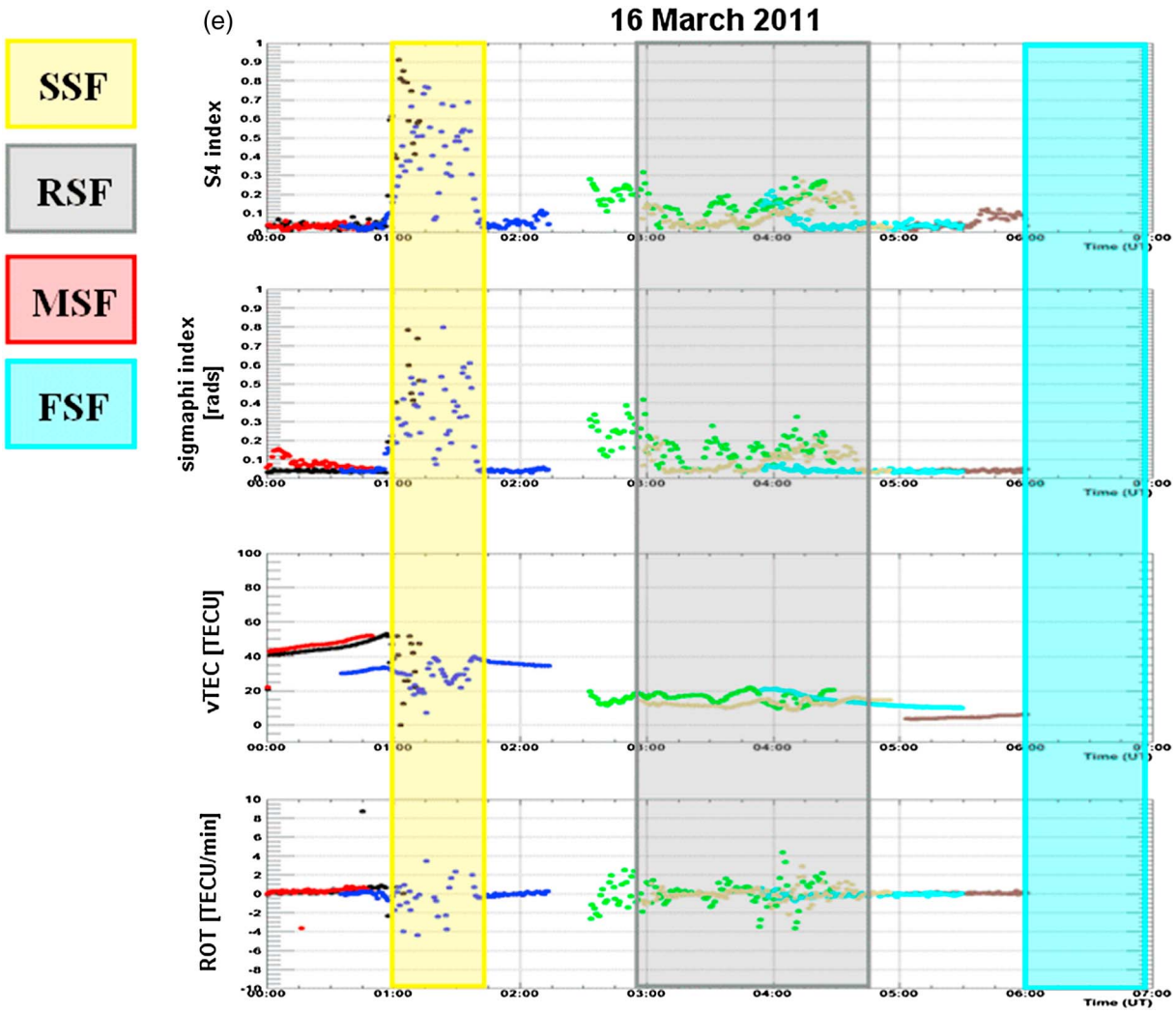

Figure 6. (a) S_4, σ_Φ , *v*TEC, and ROT values recorded on 12 March 2011 from 00:00 UT to 07:00 UT. Different colored dots mean data recorded from different satellites: black is PRN3, red is PRN6, green is PRN11, blue is PRN19, brown is PRN 20, cyan is PRN 23, and light brown is PRN 24. The ESF occurrence is highlighted with different color bars. (b) Same as Figure 6a but for 13 March 2011. In contrast with those observed on 12 March 2011, neither S_4 or σ_Φ values exceed the corresponding scintillation threshold (0.25 and 0.25 rad, respectively) nor ESF phenomena are present. (c) Same as Figure 6a but for 14 March 2011. ESF and scintillation phenomena are present. (d) Same as Figure 6a but for 15 March 2011. In contrast with those observed on 14 March 2011, neither S_4 or σ_Φ values exceeding the corresponding scintillation threshold (0.25 and 0.25 rad, respectively) nor ESF phenomena are present. (e) Same as Figure 6a but for 16 March 2011. ESF and scintillation phenomena are present.

when *v*TEC presents rapid and steep electron density gradients on all the satellites in view, this being confirmed by the ROT intensity reaching more than 8 TECU/min (total electron content unit, 1 TECU = 10^{16} el m^{-2}) between 00:00 UT and 01:00 UT (20:00–21:00 LT on 11 March). In this time interval, both SSF and RSF signatures are visible on the ionograms. The complete absence of ESF and scintillations characterizes the conditions observed on 13 March (Figure 6b). On 14 March, the expected postsunset scintillation results are time shifted to later times, centered around 04:00 UT (00:00 LT), when *v*TEC results into wave-like structuring (Figure 6c). The ionospheric conditions recorded on 15 March (Figure 6d) recall those observed on 13 March (Figure 6b), while on 16 March (Figure 6e), the postsunset scintillation and SSF incidence are clearly visible just after 01:00 UT (21:00 LT on 15 March).

[28] As already mentioned, on 14 March, the *v*TEC behavior shows a wave-like configuration (Figure 6c) between about 03:00 UT and 05:00 UT (23:00–01:00 LT between 13 and 14 March). Figure 7 illustrates how the *v*TEC from all the satellites in view (PRNs 11, 23, and 24) looks like in a 3-D plot for this specific period of time. Unlike PRN 23, whose *v*TEC values do not show any significant variation, PRNs 11 and 24 are instead characterized by a well-defined wave-like oscillation of the corresponding *v*TEC values.

[29] In order to investigate deeper this data segment, we calculated the *v*TEC perturbations along the PRNs 11 and 24 arcs according to the method proposed by *Kotake et al.*

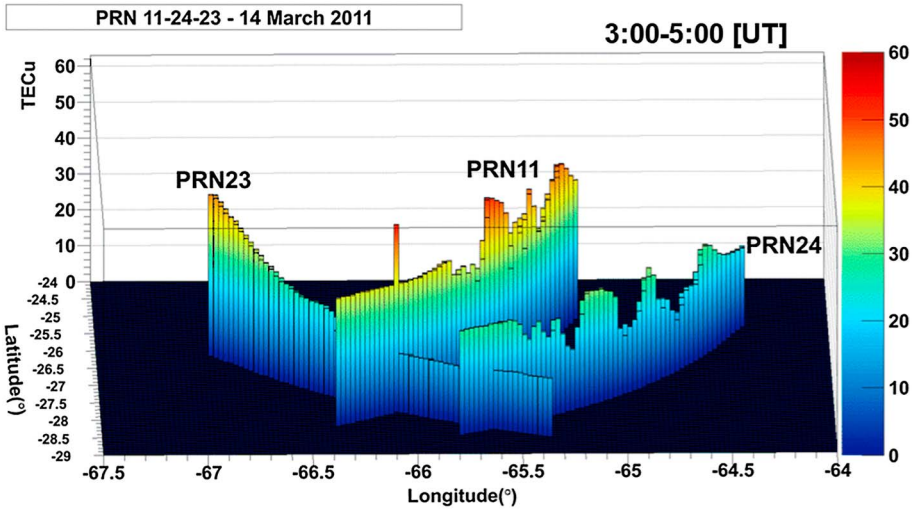

Figure 7. Three-dimensional visualization of *v*TEC values recorded on 14 March 2011 by PRNs 11, 23, and 24 from about 3:00 UT to 5:00 UT.

[2006] (Figure 8). In practice, the *v*TEC temporal sequence for each satellite-receiver pair of interest is selected, and then the *v*TEC perturbations ($v\mathrm{TEC}_{\mathrm{pert}}$) are computed by subtracting to each measured value the corresponding 1 h running mean. Thus, $v\mathrm{TEC}_{\mathrm{pert}}$ at a given time t^* is evaluated according to the following formula:

$$v\mathrm{TEC}_{\mathrm{pert}}(t*) = v\mathrm{TEC}(t*) - \langle v\mathrm{TEC}(t*)\rangle_{(-30;+30)}, \qquad (6)$$

where $v\mathrm{TEC}(t^*)$ is the measured value and $\langle v\mathrm{TEC}(t^*)\rangle_{(-30;+30)}$ is the corresponding 1 h running mean.

[30] Hence, the spectra of these perturbations are calculated with a fast Fourier transform (FFT) computed applying the Danielson-Lanczos method [*Danielson and Lanczos*, 1942]. As reported in Figure 9, a first harmonic, whose period is 42.7 min, tags both the tracks.

[31] In order to look for the possible presence of TIDs caused by GW propagation, the ionogram traces recorded at Tucumán on 14 March 2011 from 00:00 UT to 08:00 UT are manually digitized using the *Interpre* software developed by *Pezzopane* [2004], obtaining a sequence of couples of values (N, h') for each ionogram, where N is the electron density and h' is the virtual height of reflection. Then, the inversion from the ionogram trace (N, h') to the profile (N, h), where h is the real height of reflection, is performed using the POLAN technique [*Titheridge*, 1988]. From the profiles (N, h) isoheight curves $N(h = \mathrm{const} = 190, 200, 210, 220, 230, 240, 250, 260, 270, 280, 290\ \mathrm{km})$ were obtained and plotted in Figure 10. Spread-F presence from 03:00 UT to 03:45 UT and from 03:50 UT to 06:45 UT makes it impossible to correctly identify the ordinary trace to obtain the couples (N, h') needed to perform the inversion. Figure 10 shows

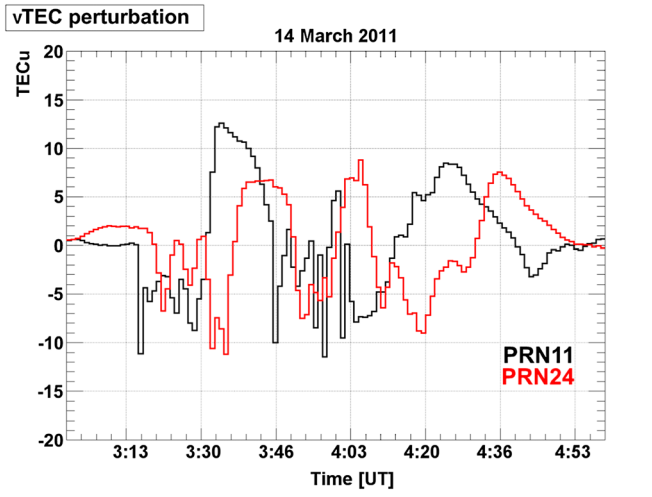

Figure 8. The *v*TEC perturbations characterizing PRNs 11 (black curve) and 24 (red curve) on 14 March 2011 from 3:00 UT to 5:00 UT.

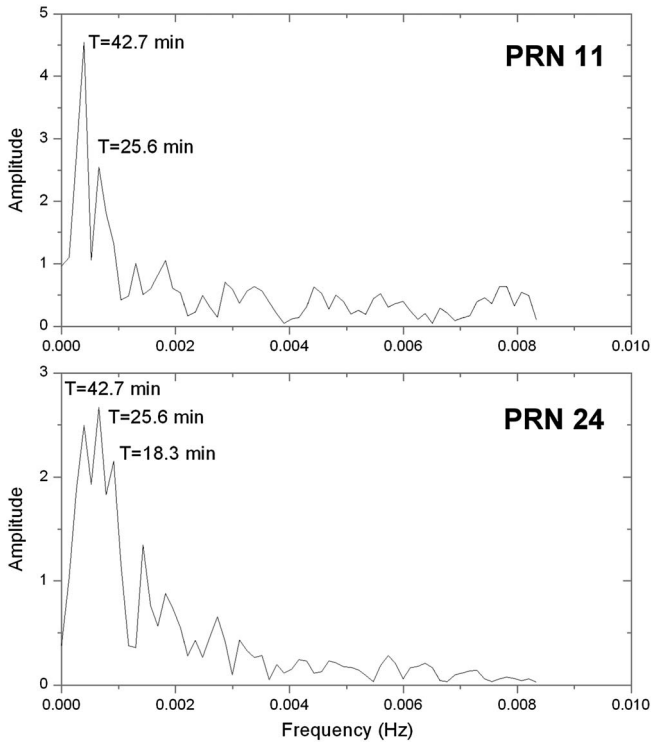

Figure 9. FFT of *v*TEC perturbations characterizing PRNs 11 and 24 on 14 March 2011 from 3:00 UT to 5:00 UT.

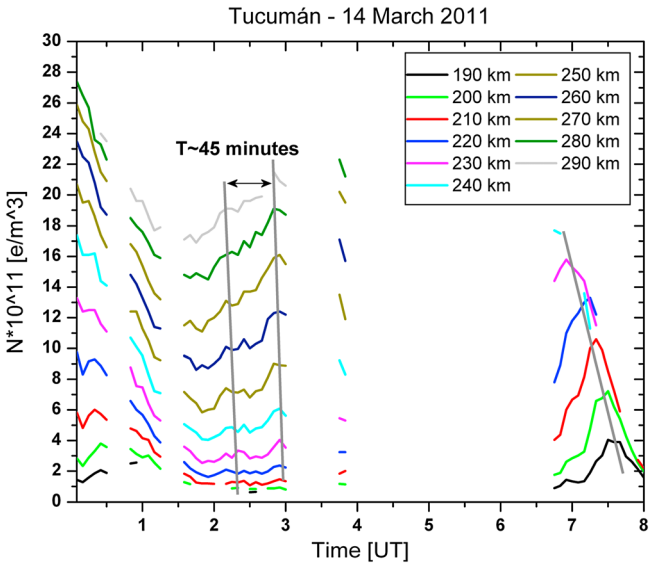

Figure 10. Electron density variations for the real height range 190–290 km computed for 14 March 2011 from 00:00 UT to 08:00 UT. Oblique gray lines highlight the downward phase shift typical of gravity wave propagation.

that from 02:00 UT to 03:00 UT, maximum N variations occur first at 290 km and then at lower heights, showing a downward phase shift which is characteristic of GW propagation in the ionospheric F region [*Hines*, 1960]. Using isoheight curves shown in Figure 10, it is possible to get an estimation of the GW period T equal to 45 min, a value comparable with that obtained from the FFT done on the vTEC perturbations and shown in Figure 9. The vertical phase velocity v_z is calculated using the peak of two consecutive heights [see *Pezzopane et al*., 2011, Figure 5], and a value of $v_z \approx 34$ m/s is found; the vertical wavelength $\lambda_z = v_z T \approx 92$ km is then obtained. These values of T, v_z, and λ_z are consistent with the analysis performed by *Klausner et al*. [2009] using a Digisonde at São José dos Campos during low solar activity. The corresponding horizontal wavelength (λ_h) can be determined using a relationship between λ_h and λ_z given by *Hines* [1960], namely, $\omega^2 \lambda_h^2 \approx (\omega_g^2 - \omega^2)\ \lambda_z^2$, where ω_g is the Brunt-Väisälä frequency, which was taken as $2\pi/14\ \mathrm{min}^{-1}$ [*Abdu et al*., 1982], and $\omega = 2\pi/T$ is the wave angular frequency. The horizontal wavelength comes out to be $\lambda_h \approx 280$ km, which is a value consistent with an MSTID.

[32] The second case here reported considers a period that looks like quiet (23, 24, and 25 September 2011) if we

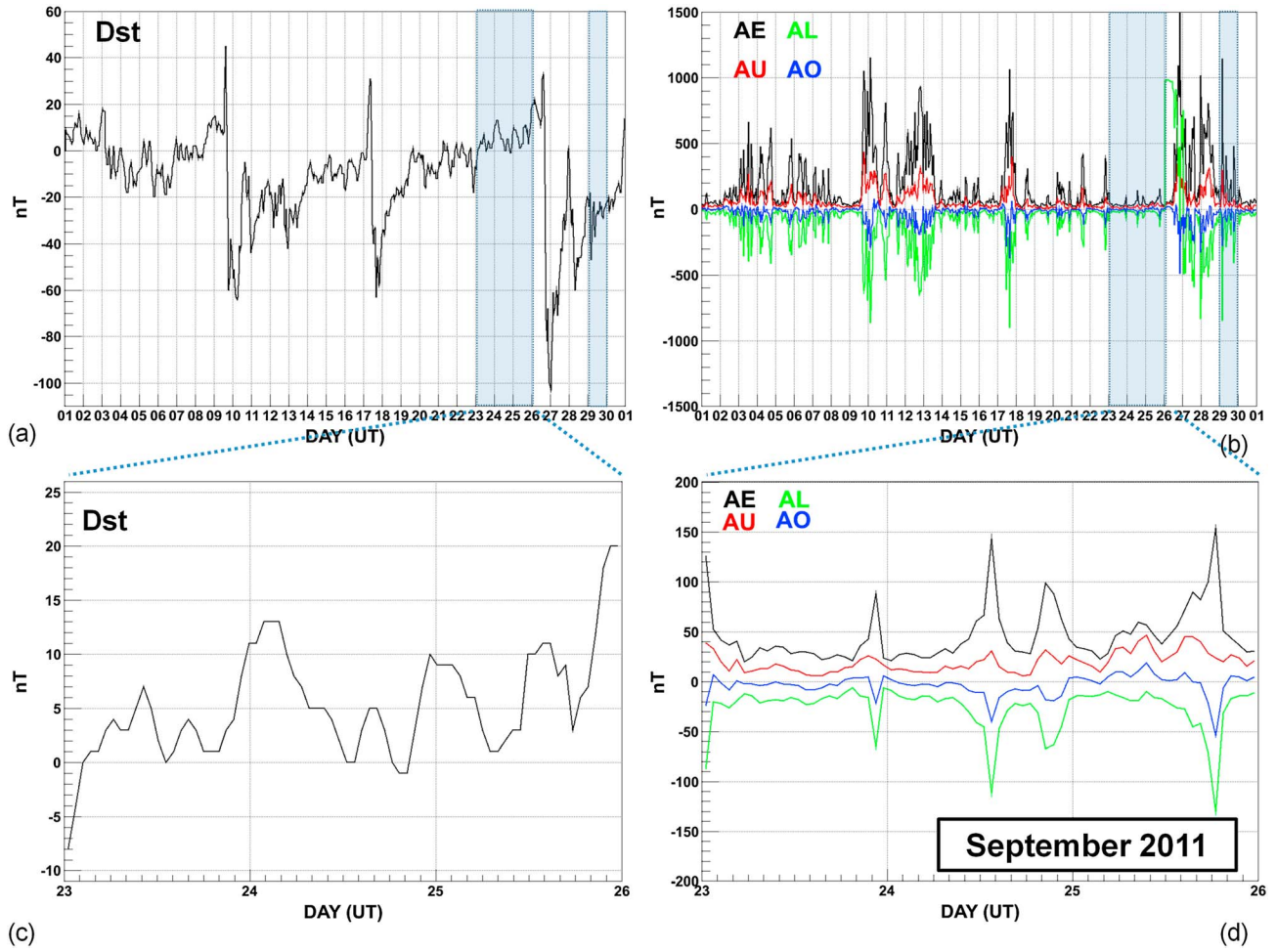

Figure 11. (a, c) *Dst* and (b, d) *AE*, *AL*, *AU*, and *AO* indices recorded in September 2011. The days from 23 to 25 September investigated in the work are shaded in Figures 11a and 11b and zoomed-in details in Figures 11c and 11d, respectively. Also, 29 September 2011 is shaded in Figures 11a and 11b but not zoomed.

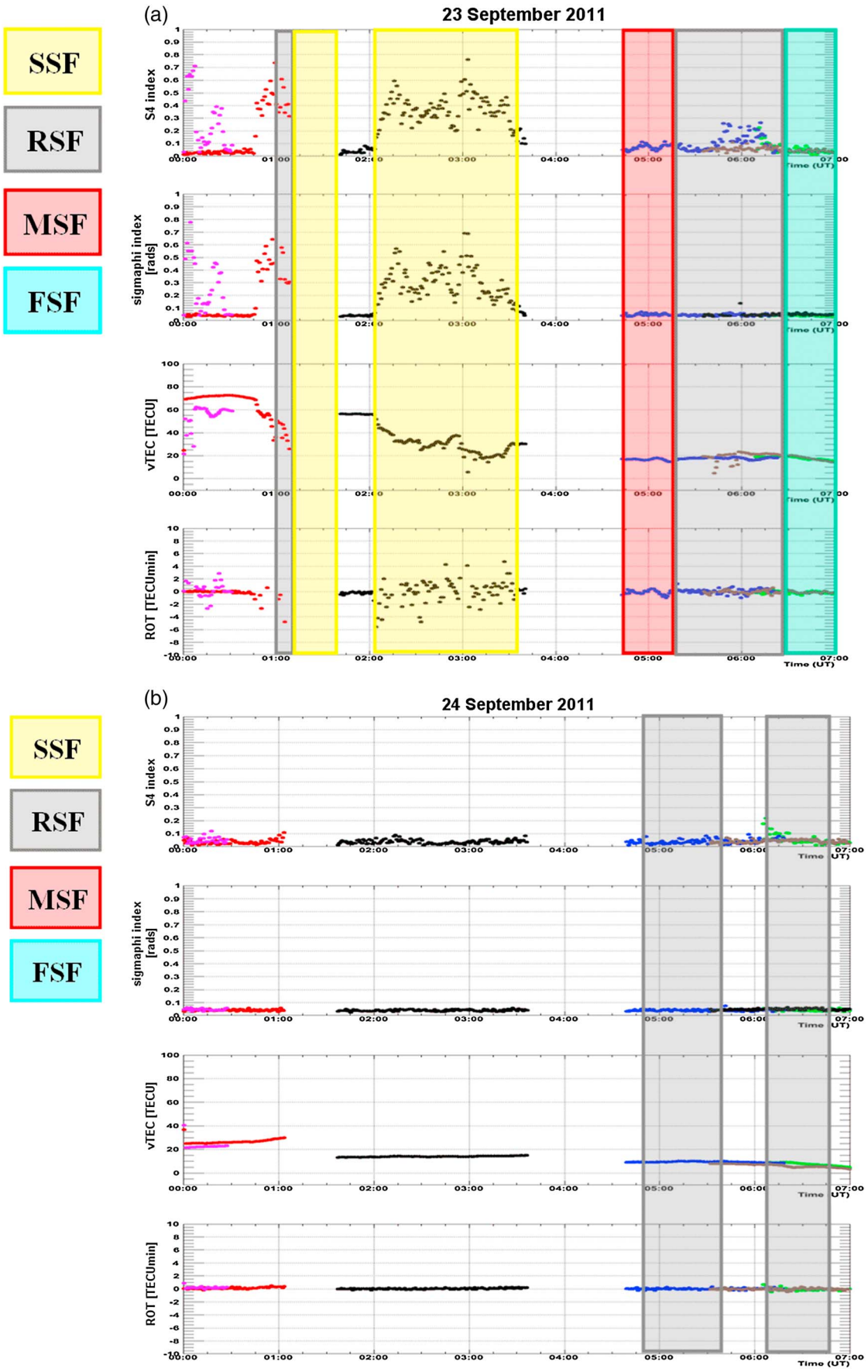
(a)
23 September 2011
SSF
RSF
MSF
FSF
S4 index
sigmaphi index [rads]
vTEC [TECU]
ROT [TECUmin]
Time (UT)
(b)
24 September 2011
SSF
RSF
MSF
FSF
S4 index
sigmaphi index [rads]
vTEC [TECU]
ROT [TECUmin]
Time (UT)

Figure 12

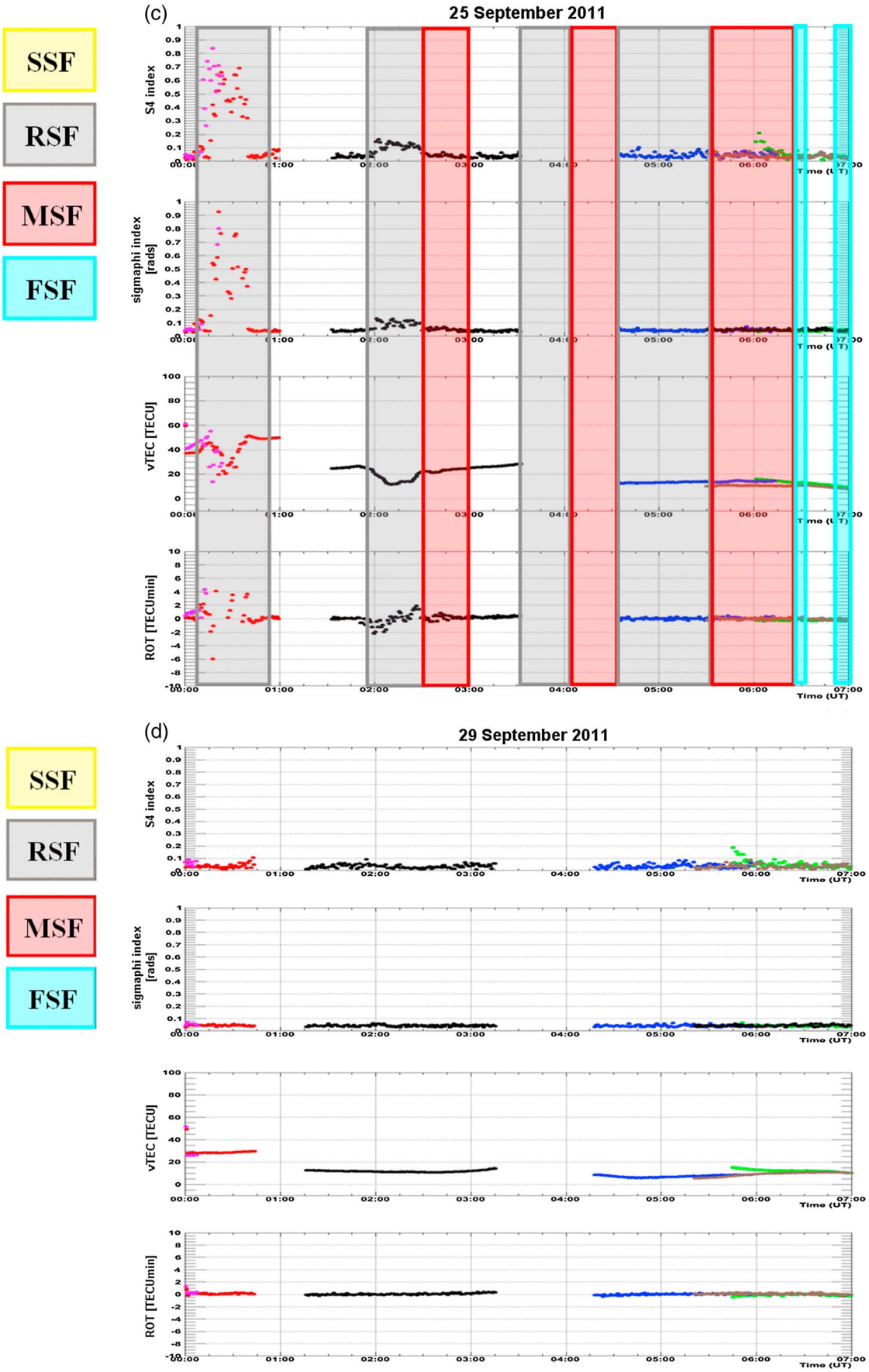

Figure 12. (continued)

consider that *Dst* ranges between −8 and +20 nT. Nevertheless, this time interval cannot be defined properly as quiet because it falls between two moderate/strong storms peaking on 17 and 26 September 2011, and it is followed by another disturbed day (29 September 2011) as illustrated by the *Dst*, *AE*, *AO*, *AU*, and *AL* indices shown in Figure 11. Again, as for the previous case, the choice of the investigated days follows the simultaneous ionosonde and GISTM data availability.

[33] The ESF and scintillation conditions are illustrated in Figure 12a–12d. Despite the fact that the considered period is not stormy (Figure 11), it presents features similar to those observed on March 2011: A strong correlation between SSF and high level of scintillations, both in phase and in amplitude, is evident on 23 September, between 02:00 UT and 03:40 UT (22:00–23:40 LT). In the previous time interval between 01:10 UT and 01:30 UT, when the SSF appears, there is no GPS satellite in view in the area probed by the ionosonde and the GISTM. Again, even though the considered period cannot be considered as disturbed, although between two storms, days characterized both by ESF and scintillations (23 and 25 September) alternate with inhibited days (only postmidnight RSF signatures of short duration characterize 24 September). Moreover, even though the ring current conditions look very different on the 2 days (Figure 11), the ionospheric conditions recorded on 29 September (Figure 12d) recall those observed on 24 September (Figure 12b).

4. Summary and Discussions

[34] Using the data recorded between October 2010 and September 2011, a period of increasing low-medium solar activity, from an AIS-INGV ionosonde and a GISTM scintillation receiver, both located at the low-latitude station of Tucumán, Argentina, near the southern crest of the equatorial ionospheric anomaly, we performed a statistics of spread-F and scintillation occurrence. Moreover, we focused on two geomagnetically fluctuating periods, both characterized by SSF and scintillations. The main features coming out from our study can be summarized as follows:

[35] 1. At low latitudes, ESF confirms to be a nighttime summer phenomenon.

[36] 2. Scintillation presents a peak at equinoxes in the postsunset sector and a minimum in winter; the bulk of the occurrence is in the postsunset and during nighttime even if amplitude scintillations result to happen also during early daytime.

[37] 3. Along the entire data set considered, but also focusing on particular case studies, the correspondence between SSF appearance and the increase of scintillation is systematic; SSF is absent in winter.

[38] 4. Correspondence between FSF and amplitude scintillation peaks at around 10:00–11:00 UT (06:00–07:00 LT) in summer and equinoxes and slightly later at 12:00 UT (08:00 LT) in winter.

[39] 5. There is the appearance of an anticorrelation between the MSF type and scintillation occurrences in all seasons, with clear evidence at equinoxes and in summer.

[40] 6. Satellite traces are confirmed to be precursors to the appearance of an RSF trace on the ionograms.

[41] 7. Both for disturbed periods and for geomagnetically quiet periods, even though between disturbed ones, ESF and scintillations days alternate with inhibited days, that is, days for which ESF and scintillations phenomena are not visible.

[42] 8. MSTIDs play an important role in generating irregularities responsible for both spread-F and scintillation signatures that are time shifted compared to the typically postsunset phenomena.

[43] Concerning points 1 and 2, the evidence that scintillation, unlike ESF, is recorded all-day long, we have to consider that several authors reported daytime scintillations caused by sporadic *E* irregularities [*Das Gupta and Kersley*, 1976; *Zou*, 2011; *Seif et al*., 2012; *Chatterjee et al*., 2013]. On the other hand, a very recent paper by *Joshi et al*. [2013] highlighted the role of the *E* sporadic (*E*s) in the genesis of equatorial plasma bubbles also during nighttime. Our results indicate that the daytime amplitude scintillations are concentrated in the interval 09:00–14:00 UT (05:00–10:00 LT) (Figure 3), when *E*s layers are often observed by the AIS-INGV ionosonde. Examples of this are given in Figures 13 and 14 showing, respectively, an S_4 enhancement between 12:30 UT (8:30 LT) and 12:40 UT (08:40 LT) on 16 November 2010 and between 12:00 UT (08:00 LT) and 12:20 UT (08:20 LT) on 30 September 2011, corresponding to an *E*s layer appearance in the related ionograms recorded by the ionosonde. From the sequence of ionograms shown in Figures 13 and 14, it is worth noting how the *E*s layer becomes "scintillation effective" when dense (not patchy) and its critical frequency approaches the value of 4 MHz, in good agreement with what was reported by *Das Gupta and Kersley* [1976]. The statistical correspondence between *E*s layer appearance and moderate amplitude scintillations is beyond the scope of the present paper, and it will be considered in a companion paper in preparation. The equinoctial scintillation peak can be explained according to *Tsunoda* [1985]: Scintillation maximizes at times of the year when the solar terminator is most nearly aligned with geomagnetic flux tubes.

[44] Point 3 represents a confirmation, on a different hemisphere, of what *Shi et al*. [2011] presented in their work based on Hainan (109.1°E, 19.5°N; magnetic latitude 9°N) data in China.

[45] Point 4 is a very intriguing feature. GPS amplitude scintillations happen when the signal encounters irregularities of horizontal dimensions up to of hundreds of meters, while phase scintillations take place also when the irregularities are of wider scales [*Aarons*, 1997; *Hunsucker and Hargreaves*,

Figure 12. Different colored dots mean data recorded from different satellites: black is PRN9, red is PRN15, green is PRN21, blue is PRN25, pink is PRN26, and brown is PRN30. (a) Same as Figure 6a but for 23 September 2011. ESF and scintillation phenomena are present. (b) Same as Figure 6a but for 24 September 2011. In contrast with those observed on 23 September 2011, no S_4 or σ_Φ value exceeding the corresponding scintillation threshold (0.25 and 0.25 rad, respectively) and only postmidnight RSF signatures of short duration are visible. (c) Same as Figure 6a but for 25 September 2011. ESF and scintillation phenomena are present. (d) Same as Figure 6a but for 29 September 2011. Neither S_4 or σ_Φ values exceeding the corresponding scintillation threshold (0.25 and 0.25 rad, respectively) nor ESF phenomena are present.

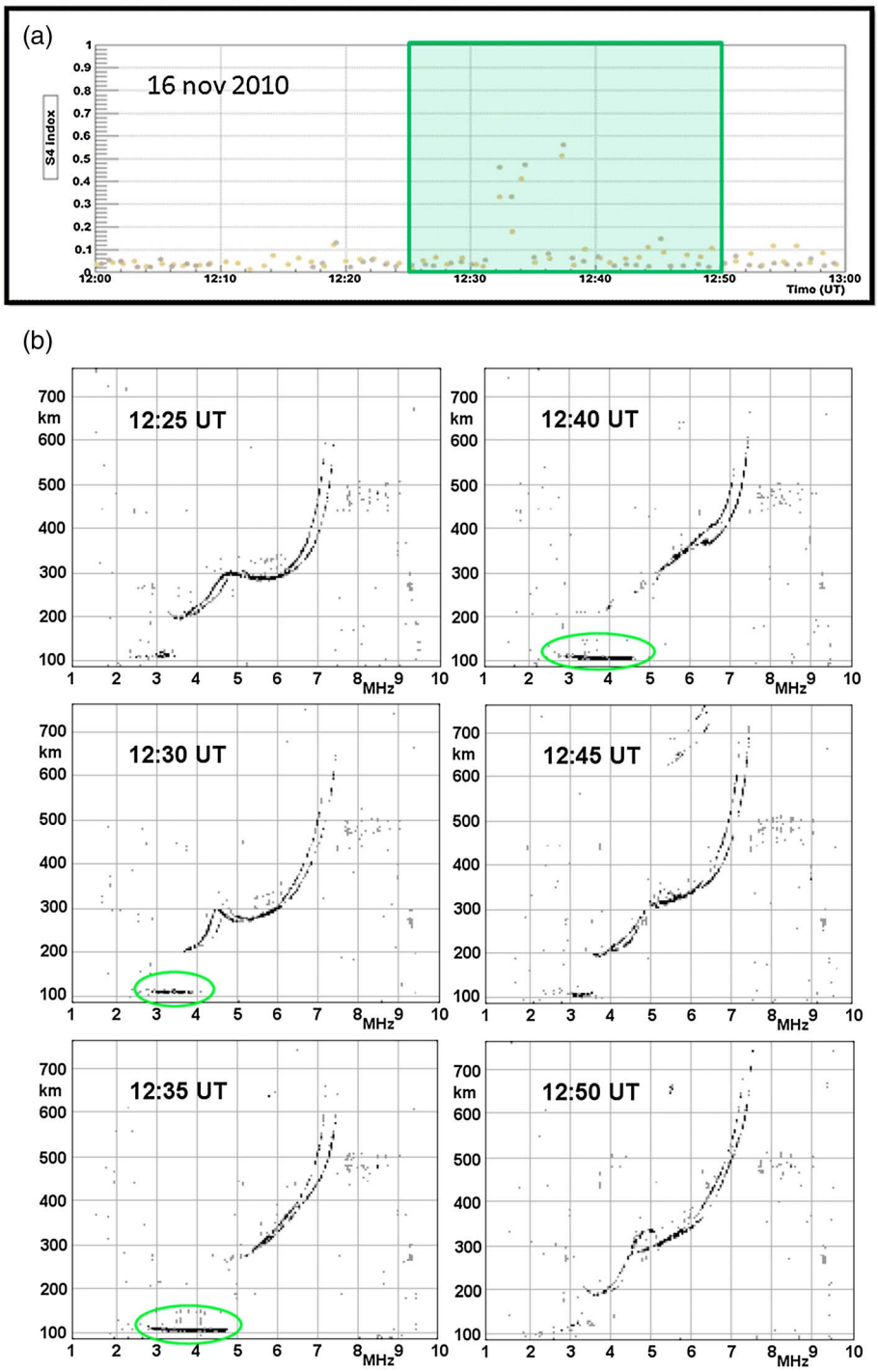

Figure 13. (a) S_4 temporal series showing moderate scintillations between 12:30 UT and 12:40 UT and (b) the corresponding sequence of ionograms, along the time interval related to the green-shaded rectangle in Figure 13a and showing the development and decay of an *E*s layer, recorded on 16 November 2010. The most pronounced *E*s layers (highlighted by green ellipses), with a critical frequency equal or greater than 4 MHz, are clearly visible in the ionograms recorded at 12:30 UT, 12:35 UT, and at 12:40 UT just as S_4 moderate scintillations are recorded.

2003]. The correspondence with FSF would mean that the bottomside irregularities located close to the *F* region peak have typical scale sizes up to hundreds of meters. Also, the correspondence between FSF incidence and amplitude scintillation peak is clearly confined in the sunrise local time (being centered around 07:00–08:00 LT, depending on season). This could testify to the presence of equatorial plasma bubbles, into which the irregularities can be embedded, resulting from the diurnal refilling of the topside ionosphere as described by the DMSP satellite observations [*Burke et al.*, 1979] and more recently

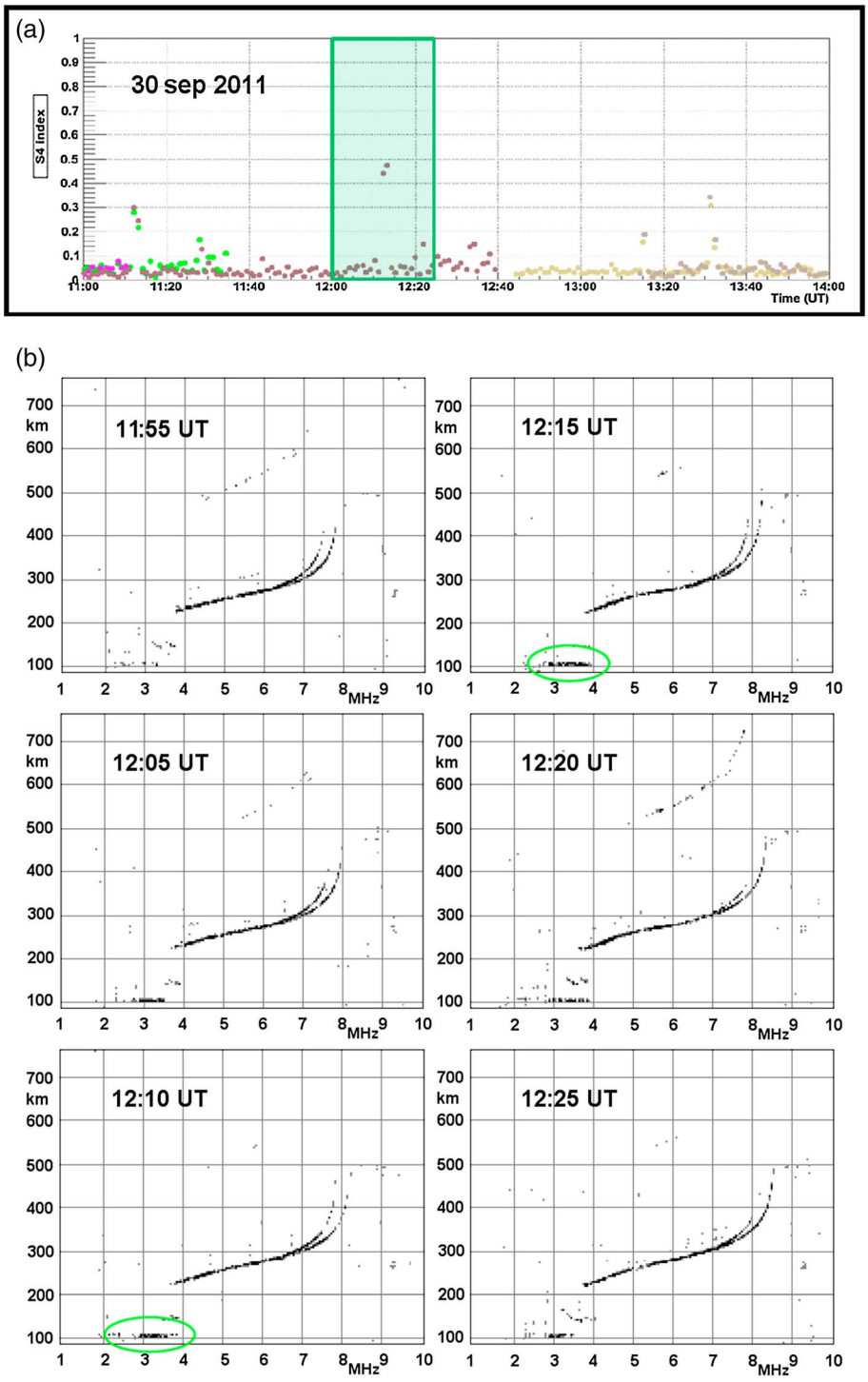

Figure 14. Same as Figure 13 but for S_4 moderate scintillations recorded on 30 September 2011 between 12:00 UT and 12:20 UT. The most pronounced and dense *Es* layers (highlighted by green ellipses), with a critical frequency of about 4 MHz, are clearly visible in the ionograms recorded at 12:10 UT and 12:15 UT, just as S_4 moderate scintillations are recorded.

by the C/NOFS satellite measurements [*de La Beaujardière et al*., 2009]. Anyhow, the correspondence needs to be further investigated and remains an outstanding question as, on the other hand, an outstanding problem in point 5 is the anticorrelation between MSF and scintillations.

[46] Concerning point 6, *Abdu et al*. [1982] were the first to investigate ST occurrence in ionograms and its possible relationship with RSF occurrence, near the southern crest of the equatorial anomaly. Recently, *Cabrera et al*. [2010] confirmed this relationship, analyzing ionograms recorded at Tucumán in 2007, and proposed a connection between RSF occurrence and GW propagation. In fact, in these cases, STs would be due to the corrugation of the isodensity surfaces caused by GW propagation which, in turn, can be

considered to be the mechanism that amplifying the postsunset seeding sources of irregularities, like the appearance of an eastward electric field during the postsunset rise of the *F* layer [*Fejer et al*., 1999; *Hysell and Burcham*, 2002; *Klausner et al*., 2009], gives rise to the instabilities responsible for the RSF signatures occurring on the ionogram. This study highlighted that when ST and/or RSF is visible on the ionogram, an increase of the scintillations indices, mainly on the signal amplitude, often occurs. Taking into account that it was found by *Cabrera et al*. [2010], this means that GWs seem to play an important role in causing irregularities responsible for both spread-F and scintillation records. This issue is also reinforced by point 8 of the summary.

[47] Point 7 is a further confirmation that scintillations can be either inhibited or triggered during disturbed periods, possibly depending on the phase of the storm and local time of occurrence of *Dst* maximum excursion [*Aarons*, 1991; *Dabas et al*., 2003]. Nevertheless, our study showed that the same alternation can characterize also days (23–25 September 2011), considered as quiet even though between disturbed ones. As argued also by *Biktash* [2004], this finding confirms the difficulty to characterize the ionospheric irregularities occurrence and related effects by using the geomagnetic indices, posing a challenge to the modelers aiming to predict ESF and scintillations conditions. From the case studies here analyzed, we also observe that S_4 and σ_Φ increases are accompanied by SSF/RSF signatures on the ionograms. This could mean that the irregularities involved are of different scale sizes and that they are mainly located at the base of the *F* region and randomly distributed along all the field of view of the ionosonde.

[48] Point 8 is a very interesting feature coming out from our investigation. The time shift to later times of the expected postsunset scintillations is consistent with the study by *Li et al*. [2011] who found that the formation of equatorial *F* region irregularities can be driven by the GW perturbations around midnight until sunrise. After becoming curious by the wave-like oscillation of the *v*TEC values characterizing 14 March 2011, we performed two independent analyses on GPS and ionosonde data. Both analyses gave as a result that the ionospheric plasma for that specific period of time was characterized by a wavy propagation whose period T is approximately equal to 45 min. Moreover, the inversion analysis from the ionogram traces let us calculate also the horizontal wavelength λ_h of the wavy propagation which resulted to be approximately equal to 280 km. Both T and λ_h are consistent with a propagation of a MSTID. Hence, this study highlights how MSTIDs can trigger irregularities responsible for both spread-F and scintillation signatures and demonstrates how a multiinstruments approach can retrieve information on GW features. As it is possible to infer from Figure 7, the identified MSTID has a wavefront elongated from northwest to southeast, which is opposite to what was illustrated both by *Makela et al*. [2010] and by *Pezzopane et al*. [2011] who found nighttime MSTIDs with wavefronts elongated from northeast to southwest. Nevertheless, it is worth noting that *Makela et al*. [2010] and *Pezzopane et al*. [2011] refer to geomagnetically quiet conditions, while here we focused on geomagnetically unstable periods. The point that MSTIDs represent an important triggering mechanism of irregularities is also confirmed by the fact that the *v*TEC wave-like behavior is concomitant with the RSF appearance, as it is possible to observe in Figure 6c. In fact, this, along with the variation practically in phase between STs and RSF signatures (see Figure 4), represents a further confirmation of a connection between RSF occurrence and MSTIDs due to GW propagation, as illustrated by *Cabrera et al*. [2010].

[49] In conclusion, it is worth highlighting that all the discussed features underlined by our analysis refer to low-medium solar activity. In order to confirm what has already been found by this study and to see whether significant differences can arise for higher levels of the solar activity, additional analyses are planned on a data set following the one we considered. Of course, these further studies will be exploited to face also the outstanding issues pertaining to the correspondence between FSF and amplitude scintillation peaks and the anticorrelation between MSF and scintillations.

[50] **Acknowledgments.** The authors thank the WDC for Geomagnetism, Kyoto, for the *Dst* and *AE* data.

[51] Robert Lysak thanks the reviewers for their assistance in evaluating this paper.

References

Aarons, J. (1991), The role of the ring current in the generation or inhibition of equatorial *F* layer irregularities during magnetic storms, *Radio Sci.*, *26*, 1131–1149, doi:10.1029/91RS00452.

Aarons, J. (1997), Global Positioning System phase fluctuations at auroral latitudes, *J. Geophys. Res.*, *102*, 17,219–17,231, doi:10.1029/97JA01118.

Abdu, M. A., I. S. Batista, I. J. Kantor, and J. H. A. Sobral (1982), Gravity wave induced ionization layers in the night *F*-region over Cachoeira Paulista (22°S, 45°W), *J. Atmos. Terr. Phys.*, *44*, 759–767, doi:10.1016/0021-9169(82)90004-6.

Abdu, M. A., E. A. Kherani, I. S. Batista, and J. H. A. Sobral (2009), Equatorial evening prereversal vertical drift and spread F suppression by disturbance penetration electric fields, *Geophys. Res. Lett.*, *36*, L19103, doi:10.1029/2009GL039919.

Abdu, M. A., I. S. Batista, B. W. Reinisch, J. W. MacDougall, E. A. Kherani, and J. H. A. Sobral (2012), Equatorial range spread F echoes from coherent backscatter, and irregularity growth processes, from conjugate point digital ionograms, *Radio Sci.*, *47*, RS6003, doi:10.1029/2012RS005002.

Alfonsi, L., G. De Franceschi, V. Romano, A. Bourdillon, and M. Le Huy (2011a), GPS scintillations and TEC gradients at equatorial latitudes on April 2006, *Adv. Space Res.*, *47*, 1750–1757, doi:10.1016/j.asr.2010.04.020.

Alfonsi, L., L. Spogli, G. De Franceschi, V. Romano, M. Aquino, A. Dodson, and C. N. Mitchell (2011b), Bipolar climatology of GPS ionospheric scintillation at solar minimum, *Radio Sci.*, *46*, RS0D05, doi:10.1029/2010RS004571.

Bagiya, M. S., and R. Sridharan (2011), Evolutionary phases of equatorial spread F including L band scintillations and plumes in the context of GPS total electron content variability: A case study, *J. Geophys. Res.*, *116*, A10304, doi:10.1029/2011JA016893.

Beniguel, Y., et al. (2009), Ionospheric scintillation monitoring and modelling, *Ann. Geophys.*, *52*(3/4), 391–416.

Biktash, L. Z. (2004), Role of the magnetospheric and ionospheric currents in the generation of the equatorial scintillations during geomagnetic storms, *Ann. Geophys.*, *22*, 3195–3202, 1432-0576/ag/2004-22-3195.

Burke, W. J., R. C. Sagalyn, R. G. Rastogi, M. Ahmed, F. J. Rich, D. E. Donatelli, and P. J. L. Wildman (1979), Postsunrise refilling of the low-latitude topside ionosphere, *J. Geophys. Res.*, *84*, 4201–4206, doi:10.1029/JA084iA08p04201.

Cabrera, M. A., M. Pezzopane, E. Zuccheretti, and R. G. Ezquer (2010), Satellite traces, range spread F occurrence, and gravity wave propagation at the southern anomaly crest, *Ann. Geophys.*, *28*(5), 1133–1140, doi:10.5194/angeo-28-1133-2010.

Cerruti, A. P., P. M. Kintner, Jr., D. E. Gary, A. J. Mannucci, R. F. Meyer, P. Doherty, and A. J. Coster (2008), Effect of intense December 2006 solar radio bursts on GPS receivers, *Space Weather*, *6*, S10D07, doi:10.1029/2007SW000375.

Chatterjee, S., S. K. Chakraborty, and S. Majumdar (2013), Summer time scintillations near the transition zone of the Indian longitude sector, *J. Atmos. Sol. Terr. Phys.*, *95–96*, 102–115, doi:10.1016/j.jastp.2013.01.017.

Chen, W. S., C. C. Lee, J. Y. Liu, F. D. Chu, and B. W. Reinisch (2006), Digisonde spread F and GPS phase fluctuations in the equatorial

ionosphere during solar maximum, *J. Geophys. Res.*, *111*, A12305, doi:10.1029/2006JA011688.

Chen, W.-S., C.-C. Lee, F.-D. Che, and S.-Y. Su (2011), Spread F, GPS phase fluctuations, and medium-scale traveling ionospheric disturbances over Wuhan during solar maximum, *J. Atmos. Sol. Terr. Phys.*, *73*, 528–533, doi:10.1016/j.jastp.2010.11.012.

Dabas, R. S., L. Singh, D. R. Lakshmi, P. Subramanyam, P. Chopra, and S. C. Garg (2003), Evolution and dynamics of equatorial plasma bubbles: Relationships to E × B drift, postsunset total electron content enhancements and equatorial electrojet strength, *Radio Sci.*, *38*(4), 1075, doi:10.1029/2001RS002586.

Danielson, G. C., and C. Lanczos (1942), Some improvements in practical Fourier analysis and their application to X-ray scattering from liquids, *J. Franklin Inst.*, *233*, 435–452.

Das Gupta, A., and L. Kersley (1976), Summer daytime scintillation and sporadic-E, *J. Atmos. Terr. Phys.*, *38*, 615–618.

Davis, T. N., and M. Sugiura (1966), Auroral electrojet activity index *AE* and its universal time variations, *J. Geophys. Res.*, *71*, 785–801, doi:10.1029/JZ071i003p00785.

Fejer, B. G., L. Scherliess, and E. R. de Paula (1999), Effects of the vertical plasma drift velocity on the generation and evolution of equatorial spread F, *J. Geophys. Res.*, *104*, 19,859–19,869, doi:10.1029/1999JA900271.

Hines, C. O. (1959), An interpretation of certain ionospheric motions in terms of atmospheric gravity waves, *J. Geophys. Res.*, *64*, 2210–2211, doi:10.1029/JZ064i012p02210.

Hines, C. O. (1960), Internal atmospheric gravity waves at ionospheric heights, *Can. J. Phys.*, *38*, 1441–1481, doi:10.1139/p60-150.

Huang, C.-M. (1970), F-region irregularities that cause scintillations and spread-F echoes at low latitude, *J. Geophys. Res.*, *75*, 4833–4841.

Hunsucker, R. D., and J. K. Hargreaves (2003), *The High-Latitude Ionosphere and Its Effects on Radio Propagation*, 1st ed., Cambridge Univ. Press, Cambridge, U. K.

Hysell, D. L., and J. Burcham (2002), Long term studies of equatorial spread F using the JULIA radar at Jicamarca, *J. Atmos. Sol. Terr. Phys.*, *64*, 1531–1543.

Iyer, K. N., M. N. Jivani, B. M. Pathan, S. Shama, H. Chandra, and M. A. Abdu (2003), Equatorial spread-F: Statistical comparison between ionosonde and scintillation observations and longitude dependence, *Adv. Space Res.*, *31*, 735–740, doi:10.1016/S0273-1177(03)00047-4.

Jin, S. G., O. Luo, and P. Park (2008), GPS observations of the ionospheric F2-layer behavior during the 20th November 2003 geomagnetic storm over South Korea, *J. Geod.*, *82*(12), 883–892, doi:10.1007/s00190-008-0217-x.

Joshi, L. M., A. K. Patra, T. K. Pant, and S. V. B. Rao (2013), On the nature of low-latitude *Es* influencing the genesis of equatorial plasma bubble, *J. Geophys. Res. Space Physics*, *118*, 524–532, doi:10.1029/2012JA018122.

Kelley, M. C. (1989), *The Earth's Ionosphere*, pp. 121–143, Academic, San Diego, Calif.

Klausner, V., P. R. Fagundes, Y. Sahai, C. M. Wrasse, V. G. Pillat, and F. Becker-Guedes (2009), Observations of GW/TID oscillations in the F2 layer at low latitude during high and low solar activity, geomagnetic quiet and disturbed periods, *J. Geophys. Res.*, *114*, A02313, doi:10.1029/2008JA013448.

Kotake, N., Y. Otsuka, T. Tsugawa, T. Ogawa, and A. Saito (2006), Climatological study of GPS total electron content variations caused by medium-scale traveling ionospheric disturbances, *J. Geophys. Res.*, *111*, A04306, doi:10.1029/2005JA011418.

de La Beaujardière, O., et al. (2009), C/NOFS observations of deep plasma depletions at dawn, *Geophys. Res. Lett.*, *36*, L00C06, doi:10.1029/2009GL038884.

Lee, C. C., F. D. Chu, W. S. Chen, J. Y. Liu, S.-Y. Su, Y. A. Liou, and S. B. Yu (2009), Spread F, GPS phase fluctuations, and plasma bubbles near the crest of equatorial ionization anomaly during solar maximum, *J. Geophys. Res.*, *114*, A08302, doi:10.1029/2009JA014195.

Leitinger, R., and M. Rieger (2005), The TID model for modulation of large scale electron density model, *Ann. Geophys.*, *48*(3), 515–523.

Li, G., B. Ning, Z. Ren, and L. Hu (2010), Statistics of GPS ionospheric scintillation and irregularities over polar regions at solar minimum, *GPS Solutions*, *14*, doi:10.1007/s10291-009-0156-x.

Li, G., B. Ning, M. A. Abdu, X. Yue, L. Liu, W. Wan, and L. Hu (2011), On the occurrence of postmidnight equatorial *F* region irregularities during the June solstice, *J. Geophys. Res.*, *116*, A04318, doi:10.1029/2010JA016056.

Makela, J. J., E. S. Miller, and E. R. Talaat (2010), Nighttime medium-scale traveling ionospheric disturbances at low geomagnetic latitudes, *Geophys. Res. Lett.*, *37*, L24104, doi:10.1029/2010GL045922.

Mannucci, A. J., B. D. Wilson, and C. D. Edwards (1993), A new method for monitoring the Earth ionosphere total electron content using the GPS global network, paper presented at ION GPS-93, Inst. of Navig., Salt Lake City, Utah.

Mayaud, P. N. (1980), *Derivation, Meaning, and Use of Geomagnetic Indices*, *Geophys. Monogr. Ser.*, vol. 22, 154 pp., AGU, Washington, D. C.

Muella, M. T. A. H., E. A. Kherani, E. R. de Paula, A. P. Cerruti, P. M. Kintner, I. J. Kantor, C. N. Mitchell, I. S. Batista, and M. A. Abdu (2010), Scintillation-producing Fresnel-scale irregularities associated with the regions of steepest TEC gradients adjacent to the equatorial ionization anomaly, *J. Geophys. Res.*, *115*, A03301, doi:10.1029/2009JA014788.

Pezzopane, M. (2004), Interpre: A Windows software for semiautomatic scaling of ionospheric parameters from ionograms, *Comput. Geosci.*, *30*, 125–130, doi:10.1016/j.cageo.2003.09.009.

Pezzopane, M., P. R. Fagundes, L. Ciraolo, E. Correia, M. A. Cabrera, and R. G. Ezquer (2011), Unusual nighttime impulsive f_oF_2 enhancement below the southern anomaly crest under geomagnetically quiet conditions, *J. Geophys. Res.*, *116*, A12314, doi:10.1029/2011JA016593.

Piggott, W. R., and K. Rawer (1972), URSI Handbook of Ionogram Interpretation and Reduction, *Rep. UAG-23A*, World Data Cent. for Sol. Terr. Phys., NOAA, Boulder, Colo.

Rino, C. L. (1979), A power law phase screen model for ionospheric scintillation: 1. Weak scatter, *Radio Sci.*, *14*, 1135–1145, doi:10.1029/RS014i006p01135.

Rodrigues, F. S., E. R. de Paula, M. A. Abdu, A. C. Jardim, K. N. Iyer, P. M. Kintner, and D. L. Hysell (2004), Equatorial spread F irregularity characteristics over Sao Luis, Brazil, using VHF radar and GPS scintillation techniques, *Radio Sci.*, *39*, RS1S31, doi:10.1029/2002RS002826.

Romano, V., S. Pau, M. Pezzopane, E. Zuccheretti, B. Zolesi, G. De Franceschi, and S. Locatelli (2008), The electronic Space Weather upper atmosphere (eSWua) project at INGV: Advancements and state of the art, *Ann. Geophys.*, *26*, 345–351, doi:10.5194/angeo-26-345-2008.

Sales, G. S., B. W. Reinisch, J. L. Scali, C. Dozois, T. W. Bullett, E. J. Weber, and P. Ning (1996), Spread F and the structure of equatorial ionization depletions in the southern anomaly region, *J. Geophys. Res.*, *101*, 26,819–26,827, doi:10.1029/96JA01946.

Seif A., M. Abdullah, A. M. Hasbi, and Y. Zou (2012), Investigation of ionospheric scintillation at UKM station, Malaysia during low solar activity, *Acta Astronaut.*, *81*, 92–101, doi:10.1016/j.actaastro.2012.06.024.

Shi, J. K., G. J. Wang, B. W. Reinisch, S. P. Shang, X. Wang, G. Zherebotsov, and A. Potekhin (2011), Relationship between strong range spread F and ionospheric scintillations observed in Hainan from 2003 to 2007, *J. Geophys. Res.*, *116*, A08306, doi:10.1029/2011JA016806.

Spogli, L., L. Alfonsi, G. De Franceschi, V. Romano, M. H. O. Aquino, and A. Dodson (2009), Climatology of GPS ionospheric scintillations over high and mid-latitude European regions, *Ann. Geophys.*, *27*, 3429–3437, doi:10.5194/angeo-27-3429-2009.

Taylor, J. R. (1997), *An Introduction to Error Analysis: The Study of Uncertainties in Physical Measurement*, Univ. Sci, Sausalito, Calif., 2nd edition.

Titheridge, J. E. (1988), The real height analysis of ionograms: A generalized formulation, *Radio Sci.*, *23*, 831–849, doi:10.1029/RS023i005p00831.

Tsunoda, R. T. (1985), Control of the seasonal and latitudinal occurrence of equatorial scintillation by the longitudinal gradient of integrated *E* region Pedersen conductivity, *J. Geophys. Res.*, *90*, 447–456, doi:10.1029/JA090iA01p00447.

Tsunoda, R. T. (2008), Satellite traces: An ionogram signature for large scale wave structure and a precursor for equatorial spread F, *Geophys. Res. Lett.*, *35*, L20110, doi:10.1029/2008GL035706.

Tsunoda, R. T., M. Yamamoto, T. Tsugawa, T. L. Hoang, S. Tulasi Ram, S. V. Thampi, H. D. Chau, and T. Nagatsuma (2011), On seeding, large-scale wave structure, equatorial spread F, and scintillations over Vietnam, *Geophys. Res. Lett.*, *38*, L20102, doi:10.1029/2011GL049173.

Van Dierendonck, A. J., J. Klobuchar, and Q. Hua (1993), Ionospheric scintillation monitoring using commercial single frequency C/A code receivers, paper presented at the Sixth International Technical Meeting (ION GPS-93), Satell. Div., Inst. of Navig., Salt Lake City, Utah, 22–24 Sept.

Wheelon, A. D. (2003), *Electromagnetic Scintillation: II. Weak Scattering*, Cambridge Univ. Press, Cambridge, U. K.

Yeh, K. C., and C. H. Liu (1982), Radio wave scintillations in the ionosphere, *Proc. Inst. Electr. Eng.*, *70*, 324–360.

Zou, Y. (2011), Ionospheric scintillations at Guilin detected by GPS ground-based and radio occultation observations, *Adv. Space Res.*, *47*, 945–965, doi:10.1016/j.asr.2010.11.016.

Zuccheretti, E., G. Tutone, U. Sciacca, C. Bianchi, and B. J. Arokiasamy (2003), The new AIS-INGV digital ionosonde, *Ann. Geophys.*, *46*(4), 647–659.